This is to certify that the
thesis entitled

QUANTIFYING THE SPECIFIC CONDUCTIVITY OF CONTAMINATED GROUNDWATER USING GROUND PENETRATING RADAR AT THE FORMER WURTSMITH AIR FORCE BASE, OSCODA, MICHIGAN

presented by

JOHN DAVID MOSS

has been accepted towards fulfillment
of the requirements for the

M.S. degree in Geological Sciences

David Hyndman
Major Professor's Signature

12/8/04
Date

QUANTIFYING THE SPECIFIC CONDUCTIVITY OF CONTAMINATED GROUNDWATER USING GROUND PENETRATING RADAR AT THE FORMER WURTSMITH AIR FORCE BASE, OSCODA, MICHIGAN

By

John David Moss

A THESIS

Submitted to
Michigan State University
in partial fulfillment of the requirements
for the degree of

MASTER OF SCIENCE

Department of Geological Sciences

2004

ABSTRACT

QUANTIFYING THE SPECIFIC CONDUCTIVITY OF CONTAMINATED GROUNDWATER USING GROUND PENETRATING RADAR AT THE FORMER WURTSMITH AIR FORCE BASE, OSCODA, MICHIGAN

By

John David Moss

A calibrated model was developed using ground penetrating radar (GPR) to quantify the specific conductivity of contaminated groundwater at the former Wurtsmith Air Force Base in Oscoda, Michigan, U.S.A., which transcends previous GPR use to image and/or delineate plume geometries based on electromagnetic (EM) wave attenuation and the observation of a 'shadow zone'. Data processing techniques consisting of: 1) editing, 2) frequency spectrum analysis, 3) band-pass filtering, 4) automatic gain control application, 5) velocity analysis, 6) normal moveout correction, and 7) spherical divergence correction are utilized to quantitatively assess the recorded GPR signals and media parameters as they relate to the propagation of EM waves. The amount of attenuation recorded in each GPR trace is calculated by assessing the exponential decay of the EM wave with increasing depth. The change in conductivity of the media between individual GPR traces is calculated using the derivative of the wave equation solved for attenuation with respect to conductivity. Empirical relationships between the electrical conductivity of groundwater and the electrical conductivity of saturated sediments, which are dependent on porosity and tortuosity, are used to calculate the specific conductivity of groundwater from the effective conductivity calculated from the GPR data. The model is calibrated to specific conductivity measurements recorded in groundwater samples collected from the on-site multi-level wells.

ACKNOWLEDGMENTS

The research is funded by a grant from the National Science Foundation Environmental Geochemistry and Biogeochemistry Program, EAR-9708487. I would like to thank David W. Hyndman for his guidance, assistance with all aspects of the project, and persevering through all obstacles, David T. Long for his guidance, assistance with project development, and field-sample collection, Phanikumar S. Mantha for his guidance and assistance with data analysis, Ran Bachrach for his assistance with geophysical interpretations and data analysis, Jennifer T. McGuire for her assistance with project development and field-sample collection, and Erik W. Smith for his assistance collecting GPR data and providing site aquifer parameters. I would like to thank Loretta, Cathy, and Jackie for their administrative guidance and assistance. I would also like to thank the National Center for Integrated Bioremediation, Research, and Development (NCIBRD) and EFX Systems, Incorporated for their cooperation.

TABLE OF CONTENTS

TABLE OF CONTENTS (continued)

LIST OF TABLES

LIST OF FIGURES

(Note: Images in this thesis are presented in color)

LIST OF FIGURES (continued)

KEY TO SYMBOLS OR ABBREVIATIONS

a	-	attenuation coefficient
A	-	amplitude
AGC	-	automatic gain control
BTEX	-	benzene, toluene, ethylbenzene, xylenes
CMP	-	common mid-point
e	-	electrical permitivity
EM	-	electromagnetic
EPA	-	Environmental Protection Agency
F	-	formation factor
FFT	-	fast Fourier transform
FTA-02	-	Fire Training Area-2
GPR	-	ground penetrating radar
k	-	wave number
K	-	dielectric constant
LNAPL	-	light non-aqueous phase liquid
μ	-	magnetic permeability
m	-	meters or cementation factor
m/s	-	meters per second
NCIBRD	-	National Center for Integrated Bioremediation Research and Development
NGVD	-	National Geodetic Vertical Datum
NMO	-	normal moveout
ns	-	nanoseconds
?	-	angular frequency
F	-	porosity
r	-	radius
redox	-	reduction / oxidation
RMS	-	root mean squared
s	-	conductivity
s_{eff}	-	effective conductivity
s_w	-	groundwater conductivity
S	-	siemens
s/n	-	signal-to-noise
t	-	time or two-way travel time
μg	-	micro-gram
U.S.G.S.	-	United States Geological Survey
V	-	velocity
V_i	-	interval velocity
V_s	-	stacking velocity
WAFB	-	Wurtsmith Air Force Base
x	-	distance or offset

CHAPTER I

INTRODUCTION

In areas where groundwater contamination is pervasive it is often difficult to identify the extent of plumes because the installation and sampling of monitoring wells is both invasive and expensive. In addition, the timeframe required for conventional contaminant plume analysis (i.e., install and sample monitoring wells and analyze the collected groundwater samples) is often on the order of weeks to months. The research presented herein provides a new mechanism to evaluate the nature and extent of groundwater contamination using remote geophysical methods from the ground surface. Information regarding the location of plume boundaries is nearly instantaneous and, with minimal data processing, the contaminant plume conditions such as specific conductivity can be accurately quantified.

This research was conducted as part of an interdisciplinary research project designed to better understand reduction/oxidation (redox) processes in a contaminant plume undergoing natural attenuation based on an interdisciplinary study of hydrogeology, geochemistry, and microbiology. The goals of the study were to (1) quantitatively assess hydrogeologic, geochemical, and microbiological constraints that influence redox processes in different regions of a plume; (2) identify sets of reactions that describe the evolution of groundwater from the water table through the contaminant plume; and (3) develop dynamic flow and transport models to explore contaminant degradation and redox processes at the site. The overall research effort offers an improved understanding of the interactions among physical, chemical, and biological processes that lead to redox zonation in both pristine and contaminated aquifers. It also provides useful information for the design of appropriate sampling, monitoring, and remediation strategies.

The analyses, results, and conclusions presented herein will supplement the larger, interdisciplinary study using a novel approach to assess contaminant plume conditions (i.e., specific conductivity) with high-resolution ground penetrating radar (GPR). The approach is based on the theory that contaminant plumes with well established microbial activity and plumes containing such contaminants as petroleum hydrocarbons, BTEX compounds (benzene, toluene, ethylbenzene, and xylenes), and chlorinated compounds, will exhibit groundwater with elevated specific conductivities as a result of ions leaching from the sediments. Organic or carbonic acids generated during microbial degradation of hydrocarbons dissolve ions such as calcium, iron, magnesium, manganese, silica, and others from the aquifer solids, which leach into the groundwater (Sauck, 2000; Atekwana, 1998; Lendvay *et. al.*, 1998; Sauck, 1998; Nash *et al.*, 1997; McMahon and Chapelle, 1991). As a result, the highly conductive groundwater significantly attenuates electromagnetic (EM) waves propagated through the subsurface by the GPR transmitting antennae, and creates what is referred to as a 'shadow zone' or 'mute zone' in a GPR profile collected through the contaminant plume (Atekwana *et. al.*, 2000; Bermejo *et. al.*, 1997).

In addition to the natural occurrence of microbial activity and the subsequent increase in groundwater specific conductivity, anthropogenic ions, most notably sodium, have been introduced to the shallow aquifer at the study site between June 1998 and June 1999. A pilot-scale pump-and-treat system designed to remediate groundwater contamination by passing it through a bioreactor was installed on-site by EFX Systems, Inc. A large amount of sodium was discharged from the bioreactor as part of the remediated groundwater returned to the study site, which also contributed to the

increased groundwater specific conductivity identified in down-gradient multi-level wells.

A calibrated site-specific model is the basis for the unique approach to analyzing GPR data for the purpose of quantitatively evaluating the specific conductivity of groundwater within a contaminant plume. Previous studies have been designed to image and/or delineate plume geometries based on GPR data rather than quantitatively assessing hydrogeologic and geochemical properties of groundwater in such complex contaminant systems. Although the approach is presented with data from the Wurtsmith site, it was developed for use on any site where GPR signal penetrates the contaminant zone and a reasonable reflector exists below the plume. The approach can be used to quickly and accurately assess a specific aspect of the groundwater quality (i.e., specific conductivity) without installing monitoring wells and collecting groundwater samples for laboratory analysis.

CHAPTER II

BACKGROUND

Although petroleum hydrocarbons as a pure phase are good insulators and exhibit low electrical conductivity values, an aquifer contaminated with dissolved phase petroleum hydrocarbons is often characterized by groundwater with elevated specific conductivity (Sauck, 2000; Atekwana, 1998; Lendvay *et. al.*, 1998; Nash *et al.*, 1997; McMahon and Chapelle, 1991). Microbial degradation of hydrocarbons creates organic or carbonic acids that dissolve ions such as bicarbonate, sulfate, nitrate, iron, manganese, silica, and others from the aquifer solids. These mobile ions leach into the groundwater and increase its specific conductivity (Sauck, 2000; Atekwana, 1998; Lendvay *et. al.*, 1998; Sauck, 1998; Nash *et al.*, 1997; McMahon and Chapelle, 1991). Microbial degradation of dissolved phase BTEX and chlorinated compounds at the research site also contributes to the formation of organic or carbonic acids and the subsequent leaching of ions from the aquifer solids. Organic acids such as benzoic, methylbenzoic, trimethylbenzoic, toluic, cyclohexanoic, dimethylcyclohexanoic, and carbonic acid have been identified during studies of petroleum spills and were each produced from aerobic and anaerobic reactions by microorganism in the subsurface (Sauck, 2000). Bacterial activity is generally greatest within areas of residual free-phase hydrocarbons near the base of the vadose zone. It has been suggested that the leachate from this zone is introduced into the underlying aquifer and/or contaminant plume during recharge events, which results in an increase in total dissolved solids and a subsequent increase in specific conductivity (Sauck, 1998).

In addition, anthropogenic sodium was introduced into the shallow aquifer at the study site between June 1998 and June 1999 during operation of a pilot-scale pump-and-treat system and bioreactor by EFX Systems, Inc. The sodium discharged from the bioreactor contributed to the increased groundwater specific conductivity identified in down-gradient multi-level wells.

The specific conductivity of the groundwater can be measured directly by analyzing water samples from a well, or, as demonstrated by this current research, estimated using GPR and subsequent data analysis. As mentioned above, highly conductive groundwater significantly attenuates EM waves propagating through the subsurface by the GPR transmitting antennae, and creates a 'shadow zone' in a GPR profile through a contaminant plume (Atekwana *et. al.*, 2000; Bermejo *et. al.*, 1997). Previous studies have suggested that the attenuation of EM waves is caused by high loss tangent scattering resulting from small, dispersed concentrations of hydrocarbons in the capillary fringe, or from contaminant vapor effects. Others have suggested that the cause is diffuse reflection resulting from the uneven water table surface due to variations in pore sizes and capillary forces, petroleum hydrocarbons, and soil mixture (Sauck *et. al.*, 1998). The current and most recognized theory is that the highly conductive waters associated with contaminant plumes with well established microbial activity attenuate the EM waves. The lack of measured reflections is not the result of a subsurface void of reflectors. Instead, it is caused by a low signal-to-noise (S/N) ratio resulting from energy scattering and absorption in the highly conductive contaminated groundwater (Yilmaz, 1987). A GPR profile collected along a transect extending from within a contaminant plume into uncontaminated background waters shows a sharp contrast from a low S/N

ratio to a high S/N ratio, respectively (Bermejo *et. al.*, 1997; Lendvay *et. al.*, 1998; Sauck *et. al.*, 1998). The use of GPR to locate contaminant plumes offers several benefits such as non-intrusive characterization of sites contaminated with hydrocarbons and chlorinated solvents (Bermejo *et. al.*, 1997), laterally extensive 2-dimensional imaging that can be acquired with relatively short time in the field, and the ability to delineate plume boundaries that may change over time due to variations in groundwater flow directions, which is not possible with stationary monitoring wells. GPR also allows for the exploration of remote places.

SITE HISTORY

The study site, also referred to as Fire Training Area-2 (FTA-02), is located at the former Wurtsmith Air Force Base (WAFB) in Oscoda, Michigan, U.S.A., which is approximately 2 kilometers west of the Lake Huron shoreline in Michigan's Lower Peninsula (Figure 1). The site was historically used for fire training exercises from 1952 to 1986. During these exercises waste fuel and solvents were ignited in the proximity of an area currently covered with a concrete pad, and were subsequently extinguished. Various compounds were used to extinguish the fires, including an aqueous film-forming foam, a multipurpose dry chemical, potassium bicarbonate based soda, and Halon 1211. Incomplete combustion of the waste fuels and solvents resulted in the infiltration of those liquids into the ground and created a large contaminant plume. In an effort to monitor the spatial and temporal changes in the distribution of contaminants within the plume migrating from FTA-02, the National Center for Integrated Bioremediation Research and Development (NCIBRD) installed a series of multi-level sampling wells. The multi-level

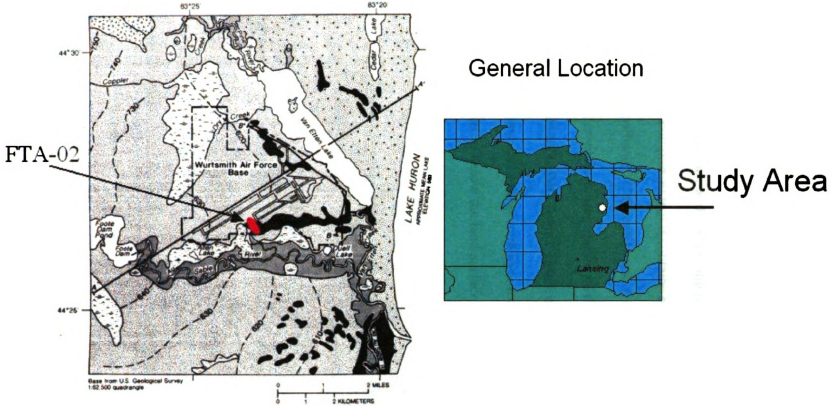

Figure 1. Study site location.

wells are generally oriented in a line perpendicular to groundwater flow approximately 100 m down gradient from the contaminant source area and were used to collect groundwater chemistry data as part of this study. The largest identified mass of contaminants occurs within the capillary fringe, but as a result of leaching, an extensive plume approximately 50 m wide and 400 m long has developed within the shallow aquifer. The plume is complex in that it contains both BTEX compounds and chlorinated solvents (e.g., dichloroethane). Concentrations of BTEX compounds in the plume range from 20 to 1,000 μg/liter while concentrations of dichloroethane, chloroethane, and vinyl chloride range from 125 to 98,940 μg/liter. Most of the contamination is associated with aquifer solids, which have an average total hydrocarbon concentration of 13,650 mg/kg between 4.5 and 5.7 meters below the land surface (USGS, 1991).

CHAPTER III

DATA ACQUISITION

HISTORICAL AQUIFER DATA

The study site is located within a shallow sandy aquifer comprised of former glacial lake sediments. Historical geologic mapping of the region has identified the entire sequence of geologic units at the site as Mississippian sandstones, siltstones and shales, overlain by unconsolidated glacial sediments and surficial deposits. The glacial deposits range in thickness from 30.5-76.2 meters and consist of gravel, sand, silt, and clay. The surficial deposits include lacustrine sediments (i.e., deltas, beaches, and lakebed sand and clay), ice-contact sediments such as till, and alluvium, which were deposited about 13,000 years ago when the water within ancestral Lake Huron was at a higher elevation. Materials from receding glaciers were transported by meltwater and deposited in the area. Aeolian deposits occur in the eastern part of the former Wurtsmith Air Force Base near Lake Huron (Stark *et. al.*, 1983; U.S.G.S., 1990). The presence of these surficial deposits has been verified by on-site well drilling activities and sediment core analyses completed by members from Michigan State University, NCIBRD, and the United States Geological Survey (U.S.G.S.).

Previous site characterization efforts included permeameter tests, slug tests, sieve analyses, and tracer tests, which demonstrated that the principal aquifer at the Wurtsmith site is a relatively homogeneous sandy unit approximately 20-meters thick, composed of sands and gravels that are highly permeable with hydraulic conductivities on the order of 30 meters/day. The homogeneity of the aquifer is later demonstrated by the distinct GPR

reflections at lithologic boundaries and the lack of reflections within homogeneous units. Permeameter measurements of two core segments collected near multi-level well ML-307 (Figure 2) yield hydraulic conductivity values of 20 and 41 meters/day. NCIBRD completed 18 slug tests on-site and calculated hydraulic conductivity values between 6 and 37 meters/day. They also completed 10 separate sieve analyses and calculated hydraulic conductivity values between 15 and 67 meters/day, with an average of 34 meters/day. In addition, a sieve analysis was completed on sediment samples collected near multi-level wells ML-3 and ML-5 (Figure 2). Using the Hazen method, hydraulic conductivity values between 15 and 38 meters/day were calculated, with an average of 26 meters/day. It was noted that there was no correlation between depth and hydraulic conductivity.

The shallow aquifer is underlain by at least 30.5 meters of silty clay, which forms a low permeability aquitard between the surficial aquifer and the underlying deeper confined aquifer. The water table ranges from approximately 4 to 6 meters below land surface (183-185 meters above sea level) and varies 0.3 to 0.7 m annually. The water table gradient ranges from 3 to 5 m/km. Assuming an effective porosity of 30%, the average groundwater velocity is approximately 0.5 m/day (McGuire *et. al.*, 2000).

GROUNDWATER GEOCHEMICAL DATA

As mentioned above, NCIBRD installed a series of multi-level sampling wells at this site to document the vertical distribution of contaminants within the on-site contaminated groundwater plume. The wells were installed as nested groups of 2.5 cm inner-diameter PVC casings with 0.33 m PVC screens set at various depths within a

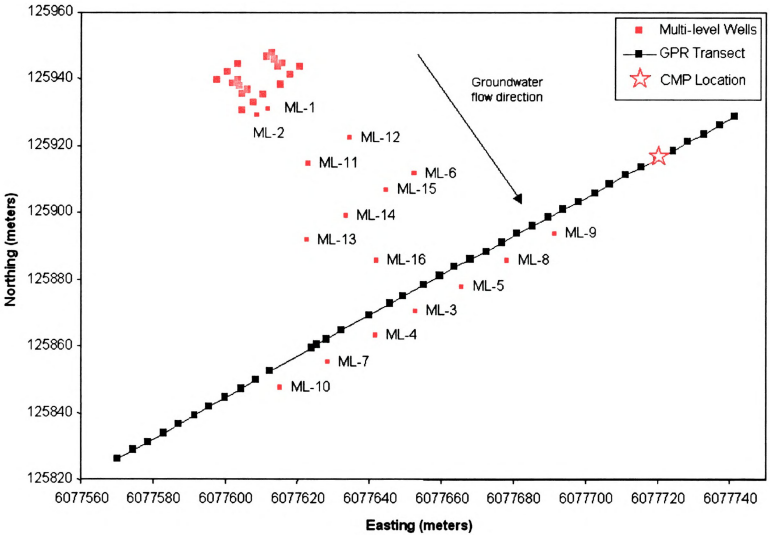

Figure 2. Multi-level wells at FTA-02 site with surveyed GPR transect.

single borehole. The vertical spacing between the multi-level screens varied from 0.5 to 2 m. A locked steel standpipe protects the PVC wells at the ground surface. Multi-level wells ML-3, ML-4, ML-5, ML-7, ML-8, ML-9, and ML-10 are oriented in a line perpendicular to groundwater flow approximately 100 m down gradient from the primary contaminant source and were used to collect groundwater chemistry data as part of this study (Figure 2). Table 1 lists the various screened depths within each multi-level well.

Table 1. Multi-level wells and screened depths below grade.

Multi-Level Well	Depth Below Grade (m)
ML-3	5.43, 5.58, 6.71, 7.63, 8.53, 9.99, 11.46
ML-4	5.33, 5.41, 6.53, 7.45, 8.36
ML-5	5.61, 5.74, 6.90, 7.82, 8.65, 10.30, 11.73
ML-7	6.39, 6.41, 8.22, 9.70, 11.20
ML-8	5.70, 5.84, 6.95, 7.88, 8.78, 10.26, 11.75
ML-9	6.52, 7.61, 8.53, 9.44, 10.91, 12.44
ML-10	6.44, 7.37, 9.75, 11.27

Groundwater Sampling Procedures and Frequency

As part of the overall project, seasonal measurements of hydrogeological, microbiological, and geochemical parameters were collected at the site and added to a dataset started in 1995 by Chapelle and others (Chapelle *et. al.*, 1996). Field personnel from Michigan State University and/or the USGS collected hydrogeological, microbiological, and/or geochemical data from the on-site multi-level wells on the following dates: 1995 (October 24), 1996 (June 13, October 24), 1997 (November 18), 1998 (February 25, April 23, May 20, June 8, August 10, November 12), 1999 (February 19, May 12, June 17, October 6), and 2000 (January 14, June 6, July 10, August 16). During each sampling event, approximately six well volumes of groundwater was purged from within each well at a rate of approximately 400 ml/min using a peristaltic pump.

Prior to sampling, the pumping rate was decreased and an in-line flow cell was attached to the tubing to continuously monitor temperature, pH, dissolved oxygen, Eh, and specific conductivity. Each parameter value was recorded every 3 to 5 minutes. Once each parameter stabilized within the flow cell, as defined by the Environmental Protection Agency's (EPA's) low-flow sampling guidance documentation, groundwater samples were collected (McGuire *et. al.*, 2000). Hydrogen (H_2) samples were collected using the bubble-stripping method (McGuire *et. al.*, 2000, Chapelle and McMahon, 1991). Following stabilization of parameters recorded by the in-line flow cell, groundwater samples were collected for extensive geochemical analysis including dissolved sulfide and iron II (Fe II) by colorimetric analysis, major cations by flame atomic adsorption, sulfate (SO_4) by capillary electrophoresis and methane (CH_4) by headspace extraction on a DOC analyzer. When applicable, samples were filtered through 0.45 μm filters. In addition, field blanks were collected during each sampling event (McGuire *et. al.*, 2000). Groundwater elevation data were collected from three hourly recording pressure transducers triangulated approximately 300 m apart about the FTA-02 site and individual water level measurements were collected manually from each available multi-level well (about 20 wells) during each sampling event.

It is important to note that despite the large amount of geochemical data collected from the site, the model presented herein only includes specific conductivity data collected in May 1999 and June 2000. The in-line flow cell was used to measure the specific conductivity of the groundwater. The conductivity of a solution, including groundwater, is highly dependent on temperature. Therefore, conductivity measurements are often immediately compensated for temperature dependence and reported as specific

conductivity so any changes in value regardless of changes in temperature may be noted. Raw conductivity measurements were compensated to 25°C using the following equation:

$$Specific\_Conductivity(25°C) = \frac{Conductivity}{1 + TC * (T - 25)} \quad (1) \text{ (YSI Incorporated)}$$

where TC is the temperature coefficient. A temperature coefficient of 1.91%/°C was used, which is an approximation for a solution containing pure KCl in water. However, this temperature coefficient also provides close approximations for calculating the specific conductivity of groundwater containing other similar salts and ions (YSI Incorporated).

GPR DATA ACQUISITION

Most GPR data for this study were acquired with a Sensors and Software® Pulse Ekko 100 system with the specifications listed in Table 2.

Table 2. Pulse Ekko 100 system specifications.

Transmitting and receiving antenna frequency	50 MHz
Transmitting and receiving voltage	400 volts
Recording scan time	1200 nanoseconds (ns)
Stacking	32-fold

Data were collected and processed using Pulse Ekko hardware and software and an in-field laptop personal computer (PC) was used as a graphical interface. A small amount of data were collected using 100 MHz antennae. Figure 3 shows a comparison of two GPR transects from the same location using 50 MHz and 100 MHz antennas. Each data set has been filtered and an automatic gain control has been applied (see below for data processing details). The two data sets appear very similar with the following exceptions:

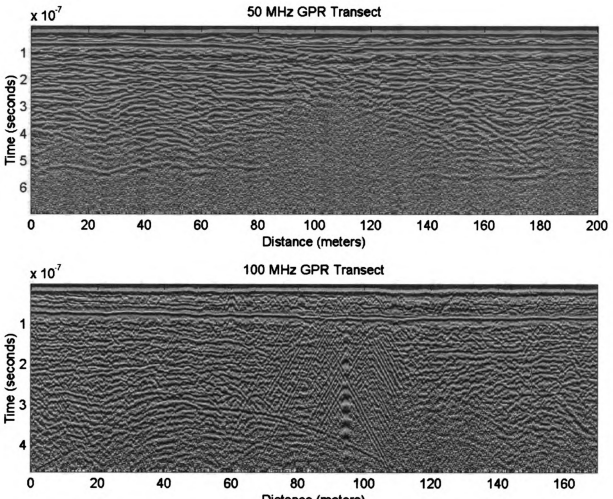

Figure 3. GPR data collected using 50 MHz and 100 MHz antennas.

1) the 100 MHz antennas provide greater resolution of the reflection events, and 2) the 100 MHz antennas do not penetrate as deep into the subsurface due to the preferential attenuation of the higher frequencies. Therefore, the 100 MHz antennas were unable to detect the clay layer at approximately 20 m below the surface. All remaining data analyses presented herein will utilize data obtained from the 50 MHz antennas.

GPR data were acquired along numerous transects across the FTA-02 site using the Pulse Ekko 100 equipment. Many transects were oriented in an east-west direction, which is perpendicular to the groundwater flow direction. Therefore, those GPR transects provide a cross-sectional "view" of the subsurface, and subsequently a cross-sectional "view" through the on-site contaminant plume. Additional transects were oriented north-south, which is parallel to the groundwater flow direction. The data analysis presented herein focuses on the GPR survey completed along a 200 m transect located immediately up gradient of the series of multi-level monitoring wells installed by NCIBRD (Figure 2). The location was selected based on its proximity to the transect of wells that lie perpendicular to groundwater flow direction and the abundant geochemical database associated with these wells as a result of temporal groundwater sampling.

During data acquisition along this transect, which is referred to as a common shot gather, the transmitting and receiving antennas were separated by 2-meters. Between points of data acquisition (a.k.a. shots) each antenna was moved 0.5-meters in the same direction along a measuring tape extended along the ground between the start and finish points of the GPR transect. The 2-meter spacing between antennas was maintained by tying a 2-meter length of rope between the antennas and drawing the string tight at each shot location. In addition, select points along the transect were surveyed to accurately

locate the transect in relation to the fire training area and the on-site wells and also establish ground elevations relative to the National Geodetic Vertical Datum of 1929 (NGVD, Figure 2). The antennas were manually moved and data were collected in 0.5-meter increments along the measuring tape. The antennas were placed in firm contact with the ground surface at each trace location to maximize coupling, although inherent variability in surface elevations caused differences in coupling at different points along the transect.

In addition to completing the 200-meter common shot gather, a common mid-point (CMP) shot gather was collected to analyze the velocity of the soils. The CMP was centered at a point corresponding to 175-meters along the 200-meter transect, which is indicated by a yellow star in Figure 2. During completion of the CMP shot gather, the initial antenna separation was 2-meters and at each successive time step the antenna offset was increased by 0.5-meters (i.e., each antenna was moved 0.25-meters away from the center point). Once again, a measuring tape was used for accurate antenna spacing and the antennas were placed in firm contact with the ground surface at each shot location to maximize coupling. Analytical methods for interpreting the GPR data and the subsequent results are presented below.

CHAPTER IV

DATA ANALYSIS

Previous studies designed by others to image and/or delineate plume geometries based on GPR data collected at the FTA-02 site and other sites often only present the graphical results of the survey. The observation of a 'shadow zone' is interpreted as indicating the presence of contaminated groundwater. However, further work to quantify the attenuation of the EM wave front and calculate aquifer and/or contaminated groundwater parameters was not completed as part of the previous studies completed by others. The data analysis techniques and the model created for quantitatively assessing the attenuation of the EM wave front as it passes through contaminated groundwater and calculating the specific conductivity of the groundwater are presented herein.

The GPR data was processed to identify the physical features (e.g. unsaturated material, saturated material, change from sand to clay) and physical properties (e.g. velocity of EM wave propagating through the material) of the underlying sediments and groundwater, with the ultimate goal of estimating the specific conductivity of the groundwater based on the level of measured signal attenuation. Conventional data processing sequences as described in Yilmaz (1987) and Sheriff and Geldart (1995) were followed to quantitatively assess individual parameters associated with the data without losing significant information. In general, data processing consisted of the following sequence: 1) editing, 2) frequency spectrum analysis, 3) band-pass filtering to remove low and high frequency noise, 4) applying an automatic gain control (AGC), 5) velocity analysis, 6) NMO correction, and 7) correcting for spherical divergence. Information

obtained from the conventional data processing techniques was then used to quantify the amount of signal attenuation and calculate the specific conductivity of groundwater within a contaminant plume at the FTA-02 site.

All processing of acquired GPR data was completed using Matlab®, which has efficient processing capabilities and data imaging techniques that make it a useful tool for analyzing acquired GPR data. Matlab® is capable of treating entire GPR data sets as a single data matrix, which can then be mathematically analyzed using matrix functions, linear algebra, Fourier transforms, etc. Large data sets are easily managed within Matlab®. The raw data from the common shot gather and CMP gather displayed using Matlab® are shown in Figures 4 and 5, respectively (see Appendix).

EDITING GPR DATA

The first step in processing both the common shot gather and CMP data sets was to remove all data prior to the arrival of the airwave because it contains no useful information for the data analysis presented herein (Figures 6 and 7). The "time-zero", which corresponds to the initiation of data acquisition, was recorded by the Pulse Ekko software once the GPR survey began. In addition, any "bad" data traces were removed. More specifically, "bad" data traces are generally created by any number of factors such as, but not limited to, poor coupling of the antennas to the ground, antennas placed directly on a foreign object (i.e., rock, metal, etc.), or malfunction of the equipment. Any "bad" traces generated within the data sets presented herein (1 bad trace out of 476 traces for the 50 MHz data sets and 13 out of 680 traces for the 100 MHz data set) were removed by averaging the two adjacent traces (see Appendix). Averaging the adjacent

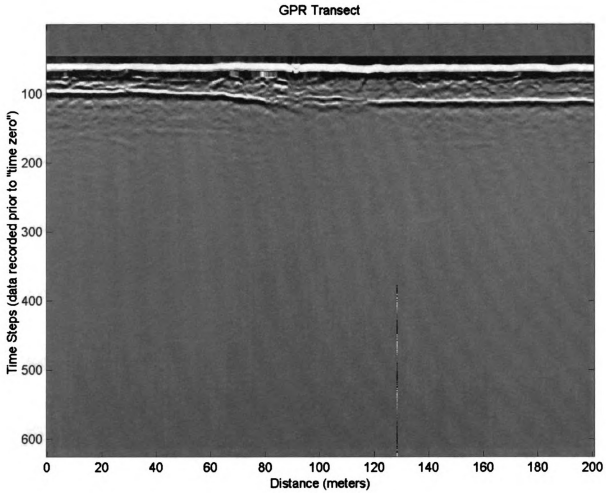

Figure 4. GPR transect at FTA-02 site, raw data.

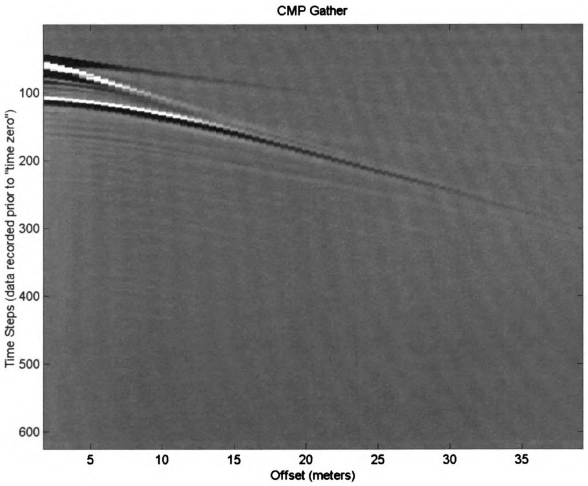

Figure 5. CMP gather at FTA-02 site, raw data.

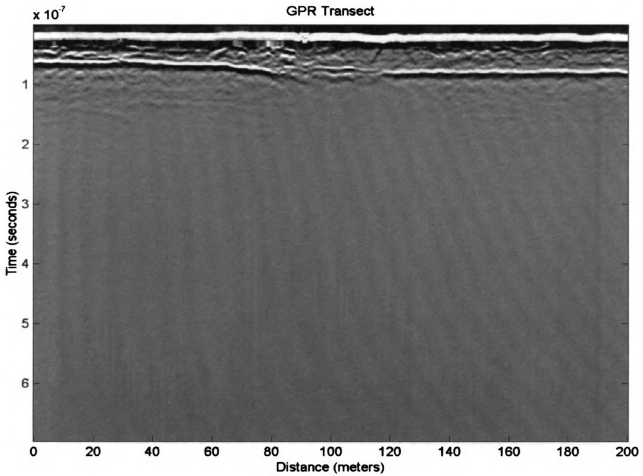

Figure 6. G GPR transect at FTA-02 site, raw data excluding bad trace and data prior to "time zero".

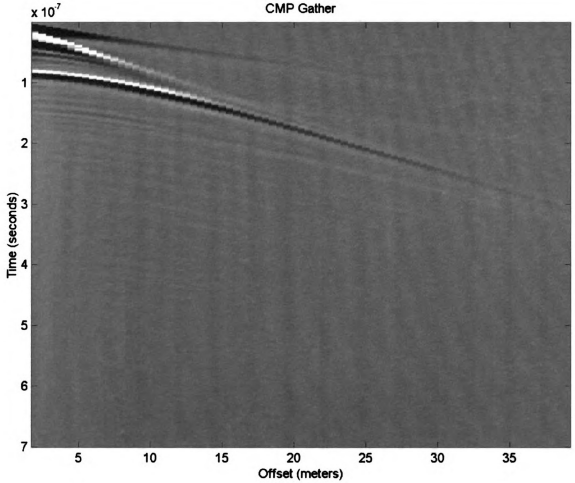

Figure 7. CMP gather along transect at FTA-02 site, raw data excluding data prior to "time zero".

data traces preserved the spatial representation of the data that would be lost by simply deleting a "bad" trace.

FREQUENCY SPECTRUM

A frequency spectrum (i.e., range of frequency components within the data) for the GPR data collected from the FTA-02 site was generated and analyzed to visually identify the very low and very high frequency components of the signal that degrade the data quality (i.e., noise). Understanding the frequency components of GPR data is necessary to filter the low- and high-frequency noise. In general, data processing can often be more easily implemented in the frequency-domain, thus the GPR signals are analyzed by converting the data from the time-domain to the frequency-domain using a forward Fast Fourier Transform (FFT). Each GPR data trace collected at a particular location is a time-dependent signal that can be uniquely and completely described as a summation of sinusoidal responses to a range of frequencies. Conversely, the synthesis of frequencies allows us to transform the data from the frequency-domain into the time-domain, which is accomplished mathematically using the inverse FFT. The significance of these operations is that no GPR data is lost or altered by changing between the time- and frequency-domains (Yilmaz, 1987).

The frequency spectrum of an individual GPR data trace was created for the GPR transect data and the CMP data set (Figures 8 and 9, respectively) to analyze the frequency components of the data. The frequency spectrum was created by transforming

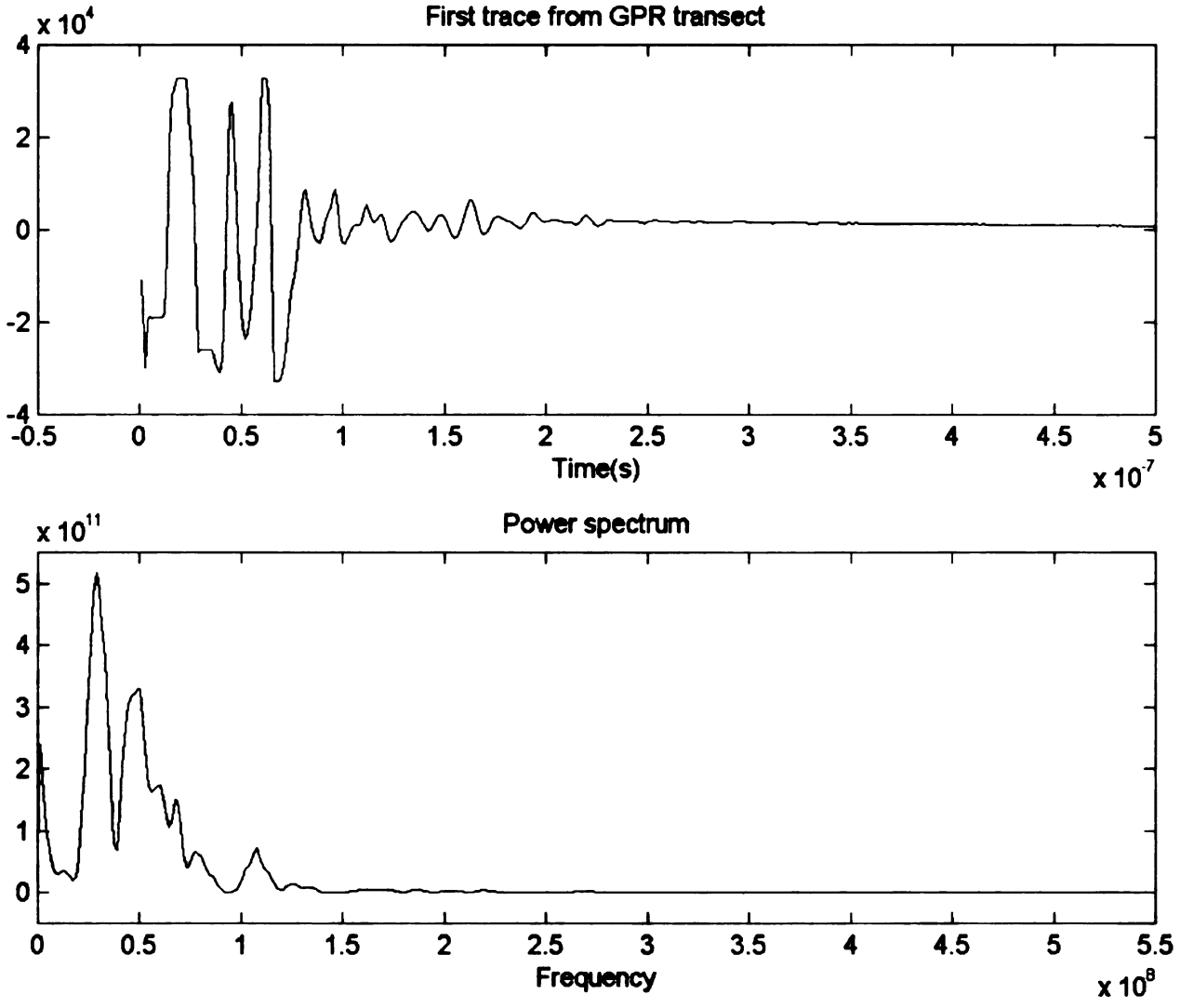

Figure 8. Representative power spectrum within GPR transect as a function of frequency.

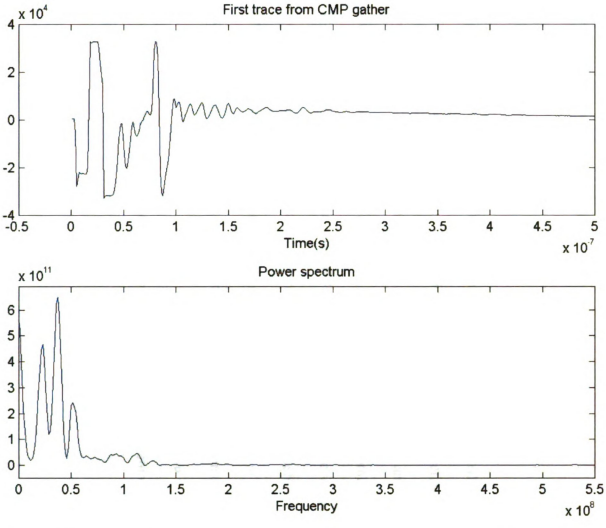

Figure 9. Representative power spectrum within CMP gather as a function of frequency..

the data trace from the time-domain into the frequency-domain by using an FFT and then multiplying the trace by its complex conjugate to obtain the real portion of the data (see Appendix). The frequency spectrum shows the individual component frequencies that comprise the entire data trace. The low and high frequency noise was then removed (i.e., filtered) from the data, as discussed below.

FILTER DATA

As mentioned above, no information is lost when data is transformed from the time-domain into the frequency-domain and vice versa using a FFT. Therefore, a data set can be transformed into the frequency-domain, edited to remove very low and very high frequency noise that degrades the data quality, and returned to the time-domain. The resultant data will be identical to the original data with the exception of the applied frequency modifications. A band-pass filter works in this manner and transforms the data into the frequency-domain, removes the unwanted frequency components of the signal, and returns the data to the original time-domain. A band-pass filter is often used because it can remove the common occurring low- and high-frequency noise present within data, thus specifying a frequency bandwidth. This process is referred to as defining a boxcar amplitude spectrum:

$A(f) = \{1, f1 < f < f2$

$A(f) = \{0,$ elsewhere (Yilmaz, 1987)

where f = frequency, f1 = minimum frequency, and f2 = maximum frequency. For the common shot gather transect completed at the FTA-02 site, the low- and high-frequency cut-off values selected were 19 and 250 MHz respectively, and for the CMP gather the values were 13 and 250 MHz respectively (see Appendix). For each data set, the low- and high-frequency cut-off values were manually selected from the frequency spectrums shown in Figures 8 and 9. In the common shot gather and CMP gather data sets, "real" data from reflections and/or direct wave arrival contains frequencies greater than 19 and 13 MHz, respectively. Therefore, lower frequency components are filtered from each data set. 250 MHz was selected as the high-frequency cut-off value because no frequency components greater than 250 MHz are present in either data set. Figures 10 and 11 show the common shot gather and CMP gather data sets, respectively, without the low- and high-frequency noise that was removed using the appropriate band-pass filter.

AUTOMATIC GAIN CONTROL (AGC)

An automatic gain control (AGC) is a scaling method applied to GPR data in which the scaling function is commonly derived from the data (Yilmaz, 1987). An AGC is often applied to GPR data for display purposes because it enhances weak reflection zones that could otherwise go unseen. However, it is important to note that an AGC-type gain destroys the original signal character and was thus only used for visualization. The GPR data collected at the FTA-02 site was visually enhanced using a root mean squared (RMS) amplitude AGC gain function, which computes the RMS amplitude within a specified time "window" on a data trace. The gain function squares the amplitude of each sample within the specified time "window" and then takes the square

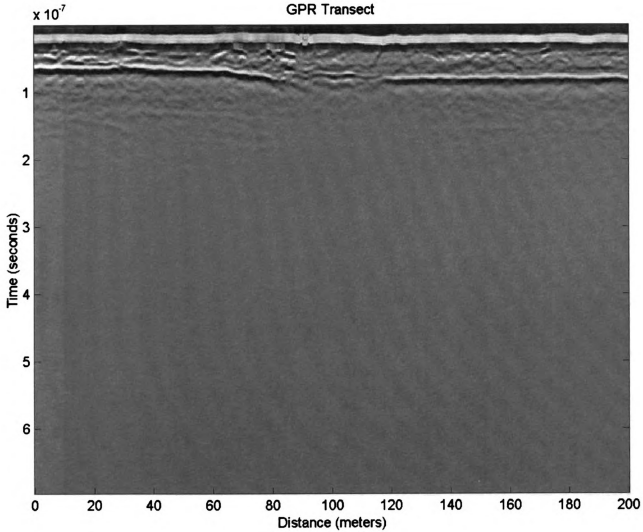

Figure 10. GPR transect at FTA-02 site, filtered.

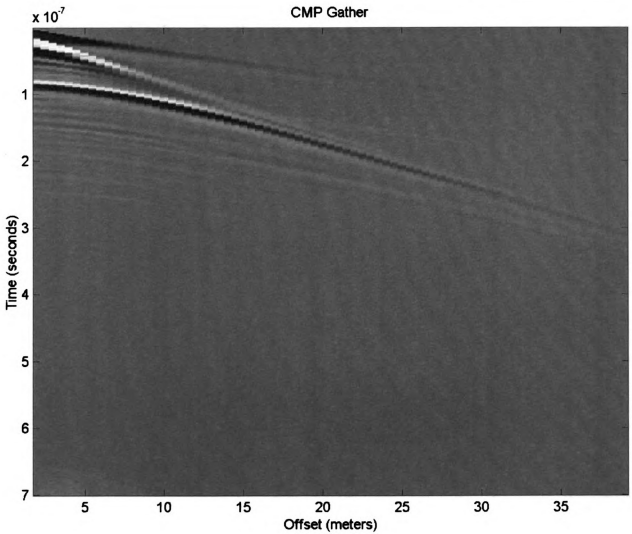

Figure 11. CMP gather at FTA-02 site, filtered.

root of the mean value, which is considered the RMS amplitude within that time "window". The RMS amplitude from each "window" along the trace comprises the gain function, which is defined for each individual data trace. The RMS amplitude values from each "window" are then interpolated to create a complete gain function equal in size to the original data trace. Dividing the original data set by the gain function, which is equivalent to normalizing the data by the RMS amplitude, completes the application of the AGC.

It is important to select the appropriate time "window" when an AGC is applied to GPR data. If the window is too small, each normalization factor used by the AGC (i.e., RMS of the data within the window) will be approximately equal to the data within the window. Therefore, the applied gain (i.e., normalization factor) will be too high within each window. As a result, variability in signal and reflection amplitudes between each window will be lost and all reflection amplitudes will appear the same. If the "window" is too large, the effectiveness of the AGC process is lessened. As the size of the time "window" increases, the gain function approaches a constant value (i.e., the RMS of the entire data set). If the applied gain function were a constant value, each data point would be divided by the same amount and there would be no net gain or loss amongst the data for visual enhancement.

The common shot gather data set was averaged over a window of 12 traces, while the CMP gather was averaged over a window of 10 traces (Figures 12 and 13, respectively), (see Appendix). The number of traces averaged as part of the AGC was selected based on visual preferences and the ability to 'see' later events in the GPR data. The AGC was applied to strengthen reflections occurring near the bottom of the GPR

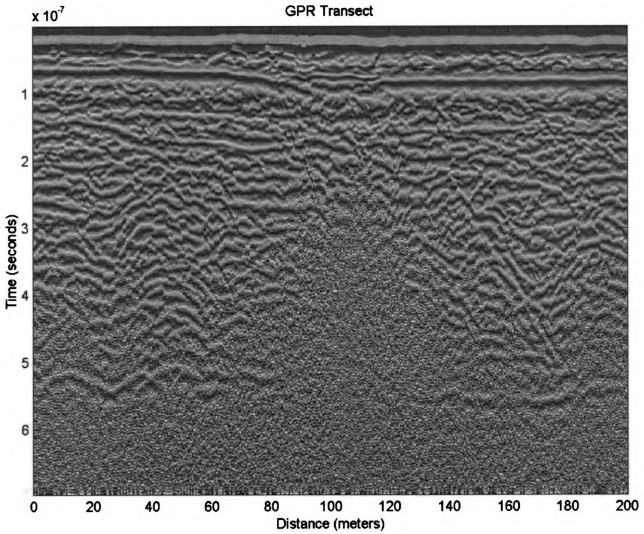

Figure 12. GPR transect at FTA-02 site with AGC applied.

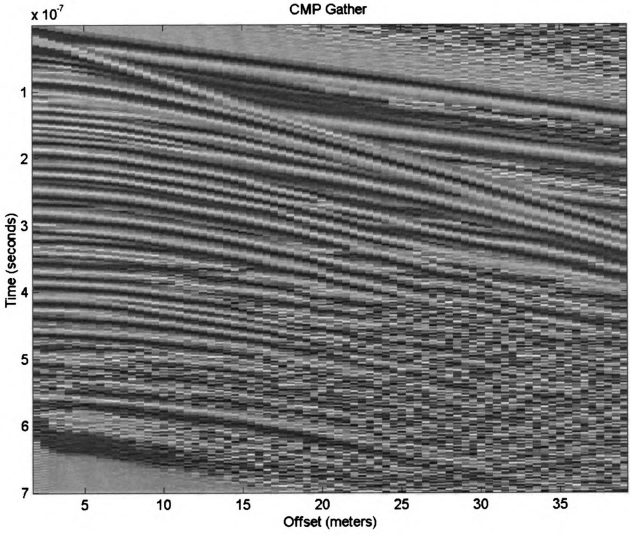

Figure 13. CMP gather at FTA-02 site with AGC applied.

transect and create a visually enhanced and revealing data set. Note that the AGC was applied to the filtered GPR data set. The 'shadow zone', corresponding to the location of the contaminant plume, can be easily seen GPR transect analyzed using an AGC. The 'shadow zone' also corresponds to the location of elevated specific conductance measured May 10-12, 1999 in groundwater from multi-level wells ML-3, ML-4, ML-5, and ML-8 (Figure 14).

VELOCITY ANALYSIS

The GPR data, as acquired in the field, records the amplitudes of various reflections as a function of two-way travel time (seconds). In order for this data to be more applicable for modeling, calculating EM wave attenuation, and calculating the specific conductivity of groundwater, it is necessary to convert the two-way travel time between the ground surface and individual reflections into depth. This transformation into real space allows for a direct comparison between physical measurements of depth to the water table, depth to the clay layer, thickness of reflective layers, and distances of wave propagation to those calculated from the GPR data. The basic principles for analyzing seismic data were used to analyze GPR data and quantitatively assess the velocity of the EM waves through the unsaturated and saturated sediments.

A quantitative assessment of GPR signal (i.e., electromagnetic waves) attenuation due to contaminated groundwater must be based on an accurate velocity analysis of the subsurface media because the amount of attenuation is a function of distance traveled by the EM wave. The velocities of the EM waves were estimated by analyzing GPR data in

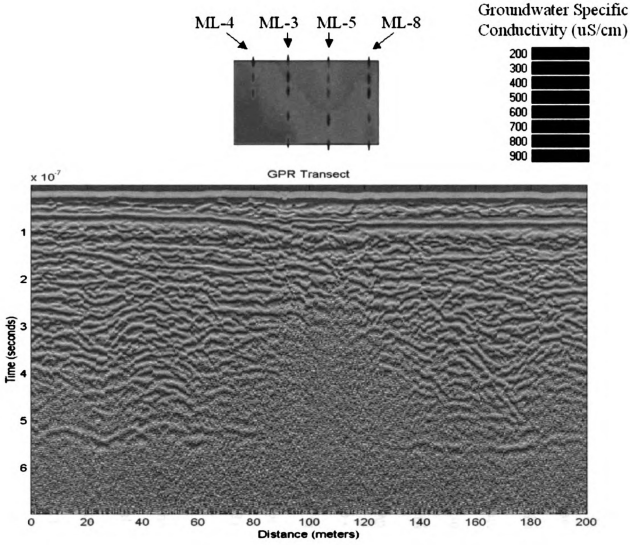

Figure 14. GPR transect at FTA-02 site with AGC applied and contoured May 1999 groundwater specific conductance data

the time-domain. The velocity estimates resulted in proper time-to-depth conversions, based on a comparison between GPR derived depths to the water table and clay layer and those measured in the field. The velocity estimates also result in proper time-to-distance conversions for the propagating EM wave, which is required to calculate the attenuation of the wave as it passes through the subsurface media.

The first subsurface layer encountered at the FTA-02 site was the unsaturated zone. The physical and/or dielectric property differences between the unsaturated and saturated soils caused a reflection at the capillary fringe above the water table, which was recorded in both the common shot gather and CMP GPR surveys. It is important to note that the EM wave reflection off the top of the capillary fringe results in a slight difference between depth to the actual water table measured in the multi-level wells on-site and the same depth calculated from the GPR data. Subsequent reflections observed in the GPR data set are the result of differences in the physical and/or dielectric properties of various stratigraphic units within the saturated subsurface sediments. The two reflectors at the FTA-02 site shown in Figure 15 are characterized as: 1) the capillary fringe, and 2) a clay unit at the base of the shallow aquifer.

A general understanding of the different types of velocity that can be estimated is required prior to performing the velocity analysis. When dealing with a horizontal layer comprised of a single-velocity media, the curve generated by plotting two-way signal travel time as a function of transmitter/receiver offset is a hyperbola (Figure 16). The difference in travel time measured at a given offset and travel time measured at zero-offset is referred to as normal moveout (NMO). The NMO velocity is therefore defined as the velocity required to correct for normal moveout and is also equal to the velocity of

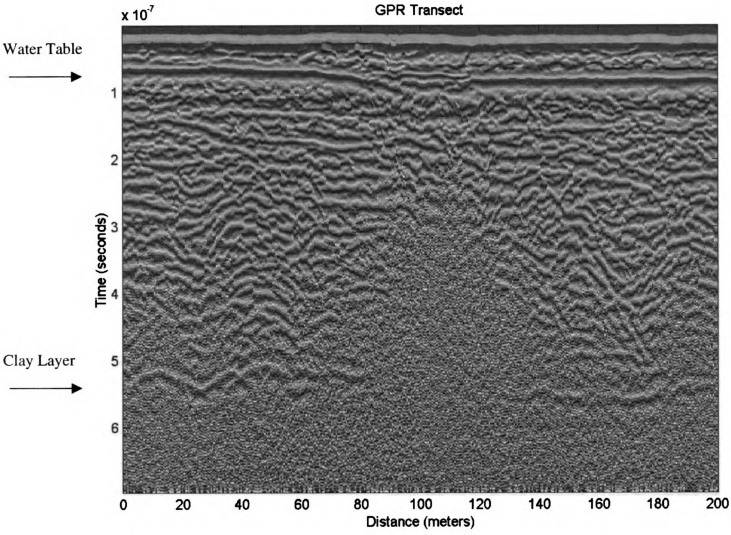

Figure 15. GPR transect at FTA-02 site with outlined reflectors.

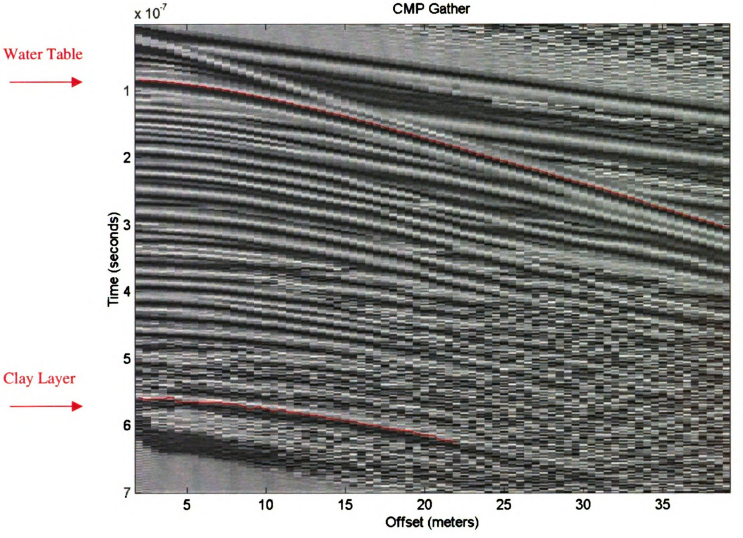

Figure 16. CMP gather centered at 175-meters along GPR transect with outlined reflectors.

the media above the reflector. If several horizontal layers are present with distinct horizontal reflectors at each layer interface, the curve generated by plotting signal travel time as a function of offset is still a hyperbola. It is important to note that the NMO velocity is calculated from the hyperbolic data set using only small offsets relative to depth. The general rule of thumb is that offsets should be kept less than the depth to a particular reflector. In addition, when only small offsets are considered, the NMO velocity for the horizontally layered media is equal to the RMS velocity of the layer being considered.

Another velocity type that is often calculated is the stacking velocity. The NMO velocity utilizes small offsets only, while the stacking velocity is equivalent to the hyperbola that best fits the entire data set. Due to the inherent similarities, NMO velocity and stacking velocity are often considered equivalent. Once again, this holds true at small offsets. The interval velocity, which is also referred to as the Dix velocity, is the average velocity within a layer or stratigraphic unit between two reflectors.

Velocity Spectrum

A common technique for analyzing any of the above-mentioned velocity types is to compute a velocity spectrum. The idea behind a velocity spectrum is to display some type of signal coherency as a function of the NMO velocity selected to "flatten" a reflector (i.e., correct for normal moveout) plotted as a hyperbola in a CMP data set. Signal coherency is calculated by summing the amplitudes within the data set along each two-way travel time. When the correct NMO velocity is selected and the hyperbola is

"flattened", the signal coherency is greatest because the positive and negative phases of the sinusoidal EM wave are aligned.

The signal coherency of the CMP data collected at FTA-02 was determined for a wide range of NMO velocity values. A velocity spectrum was created by plotting the coherency values at each two-way travel time (i.e., the sum of amplitudes at each offset distance) as a function of NMO velocity (Figure 17). Peak values corresponding to a coherent signal are shown as bright spots in the velocity spectrum. The type of media and presence of unsaturated and saturated sediments at the FTA-02 site constrained the range of velocity values used in the velocity spectrum analysis (i.e., x-axis on Figure 17). As mentioned above, if only the portion of the CMP data set comprised of small transmitter/receiver offsets relative to reflector depths are used, then the NMO velocity is equivalent to the RMS and stacking velocities (Yilmaz, 1987).

A Matlab® code was created (see Appendix) to perform velocity analyses on CMP gathers and generate a velocity spectrum. It is a universal code that can be applied to any data set as long as several basic assumptions are met (e.g. proper coupling of the antennae with the ground surface, subsurface reflectors are horizontal, etc.). The code works, as described above, by using a range of user-supplied NMO velocities to determine the "best-fit" velocity values to "flatten" the hyperbolic representation of an individual reflector. The necessary inputs into the code are the CMP data set (referred to as agx by the code), a vector of values corresponding to the incremental transmitter/receiver offset values (offset), time of the first data arrival (t1), sampling time interval (dt), minimum and maximum NMO velocity to be analyzed (vmin and vmax, respectively), increment to increase vmin by during each iteration of the calculation (dv),

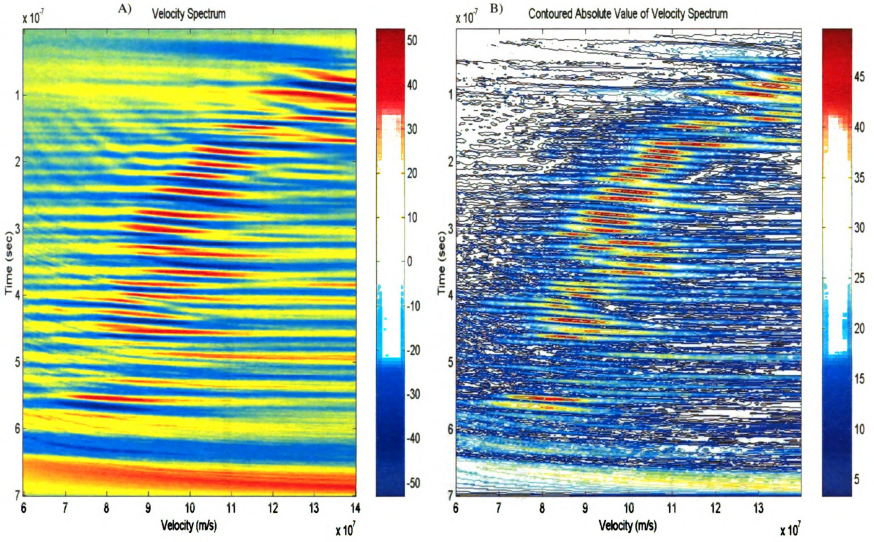

Figure 17. A) Velocity spectrum. B) Contoured image of the absolute value of the velocity spectrum.

and the mutestretch value (mutestrch). The mutestretch value truncates data corresponding to large transmitter/receiver offset values in relation to the depth to the reflector. The mutestretch value is also used to delete (mute) data within the shallow events that were stretched and subjected to frequency distortions during normal moveout velocity correction (Yilmaz, 1987). Note that the code works best using a CMP data set that has been visually enhanced by an AGC. By using a data set with an AGC applied to it, reflector strengths are enhanced and signal coherency is more prominent. The velocity analysis does not utilize the actual amplitude values of the reflections as part of its calculations. The velocity analysis only considers the coherency of signals. Therefore, using a CMP data set that has been visually enhanced by an AGC is appropriate. The output parameters generated by the code are NMO velocities (equivalent to RMS and stacking velocities) for the media above each reflector, interval velocities of the media between each reflector (calculated using the Dix equation), the two-way travel times corresponding to the initiation of each interval velocity, and the thickness of each layer. The interval velocities and their corresponding times were used to convert two-way travel times recorded in the GPR data into depths.

Results of Velocity Spectrum Analysis

For the analysis of the GPR data from the FTA-02 site, the input values into the code are listed in Table 3.

Table 3. Input values for velocity spectrum code.		
Input	**Abbreviation**	**Value(s)**
CMP data with AGC applied	agx	Data from FTA-02 site
A vector of values corresponding to the incremental transmitter/receiver offset values	offset	2 to 39 m, at 0.5 m increments
Time of the first data arrival	t1	0 seconds
Sampling time interval	dt	1.2×10^{-9} seconds
Minimum NMO velocity to be analyzed	vmin	8×10^{7} m/s
Maximum NMO velocity to be analyzed	vmax	1.394×10^{8} m/s
Increment to increase vmin by during each iteration of the calculation	dv	0.6×10^{6} m/s
Mutestretch value	mutestrch	35

The coherency image generated by the code is shown in Figure 17. The NMO velocities for the media above each of the two reflectors shown in Figures 15 and 16 were then determined from the velocity spectrum. Figures 18 and 19 show close-up images of each reflector's coherency within the velocity spectrum. In each case, points are shown on the figures that identify maximum coherency values for the positive and negative phases of the reflected electromagnetic wave. The NMO velocities corresponding to the maximum coherency values for the positive and negative phases of the individual reflector were averaged to best approximate the velocity for the zero-phase portion of the reflected electromagnetic wave. In addition, the two-way travel times corresponding to the maximum coherency values for the positive and negative phases of the individual reflector were averaged to best approximate the two-way travel time for the zero-phase portion of the reflected electromagnetic wave.

Based on this analysis, the NMO velocities for the material above each of the identified reflectors were calculated (Table 4).

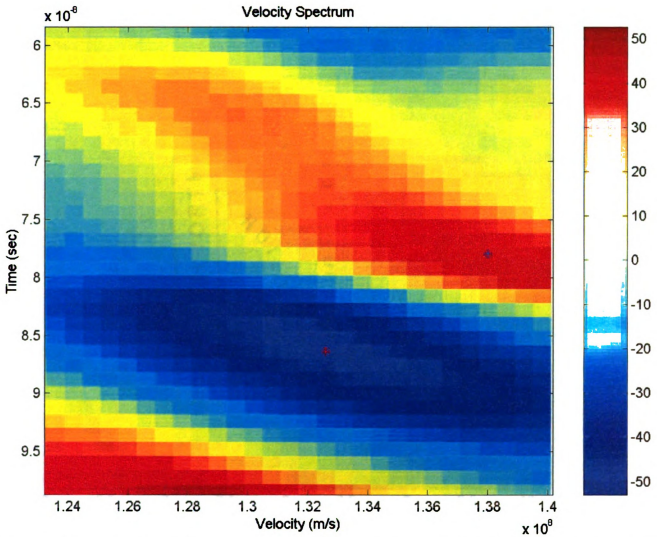

Figure 18. Points identifying locations of maximum coherency for positive and negative phases of water table reflector within the velocity spectrum.

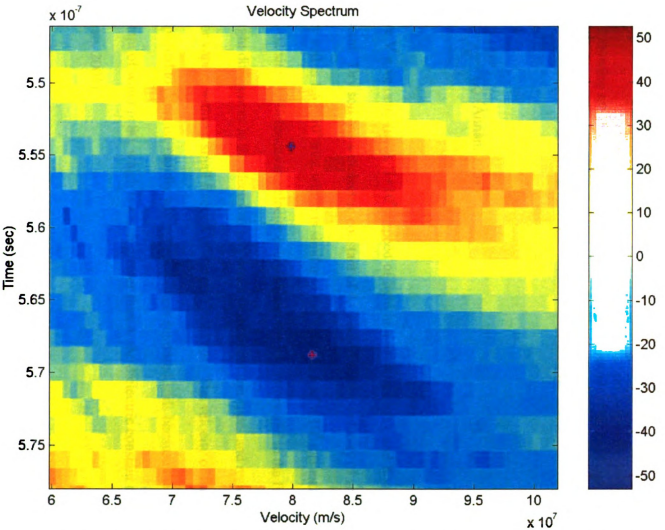

Figure 19. Points identifying locations of maximum coherency for positive and negative phases of clay layer reflector within the velocity spectrum.

Table 4. Calculated NMO velocities	
Reflector / Material Above Reflector	**NMO Velocity of Material**
Capillary fringe / Unsaturated Zone	1.35×10^8 m/s
Clay layer / Saturated and Unsaturated Zone	8.07×10^7 m/s

The following relationship was used to compare the unsaturated velocity value with that obtained in laboratory settings:

$$V = \frac{3*10^8}{\sqrt{K}} \quad (2) \text{ (Annan, 2001)}$$

where V = velocity (m/s), $3*10^8$ = speed of light in a vacuum (m/s), and K = dielectric constant. Dry soil has a dielectric constant of 4. Therefore, the velocity of an EM wave in dry soil is 1.5×10^8 m/s, which is similar to the value of 1.35×10^8 m/s estimated at the FTA-02 site. Differences in velocity calculated in the laboratory and in the field are due to slight differences in the electrical properties of different soil types and residual liquids and/or vapors within a small fraction of the pore volumes. The velocity of the EM wave is expected to decrease rapidly when it encounters saturated soils because the dielectric constant of water is 80, which is much greater than 4, the dielectric constant of soil. (Annan, 2001).

X^2-T^2 Method

A second technique used to estimate the velocity of the subsurface media from a CMP gather is the X^2-T^2 method, where x is equal to the transmitter/receiver offset

distance and t is equal to the two-way travel time of the reflected electromagnetic wave. The two-way travel time is a function of the velocity of the media above the reflector, the depth to the reflector, and the offset distance between the transmitter and receiver. This method is based on the relationship:

$$t^2 = \frac{x^2}{V_S^2 + t_0^2} \quad (3) \text{ (Sheriff and Geldart, 1995)}$$

where V_s equals the stacking velocity and t_o equals the time of the initial recorded signal (Sheriff and Geldart, 1995). If we plot t^2 as a function of x^2, and the velocity is constant, the result is a straight line with a slope of V_s^2 and a y-intercept of t_o^2. Sheriff and Geldart (1995) and Yilmaz (1987) noted that when the reflectors are horizontal and offset distances are small when compared to the depths to the reflectors, the stacking velocity calculated using the above relationship is nearly equivalent to the RMS velocity.

Results of X^2-T^2 Analysis

The two-way travel times and offset distances measured from the reflectors shown in Figure 16 were analyzed using the X^2-T^2 method to determine the velocity of the horizontal subsurface layers (Figure 20). Note that the velocities within each layer are inferred to be constant and the layers are essentially horizontal based on the high R^2 values ranging between 0.9929 and 0.9999. The calculated RMS velocities for each identified reflector are listed in Table 5. The velocities within each layer, calculated using the velocity spectrum and the X^2-T^2 method, are very similar. Each velocity

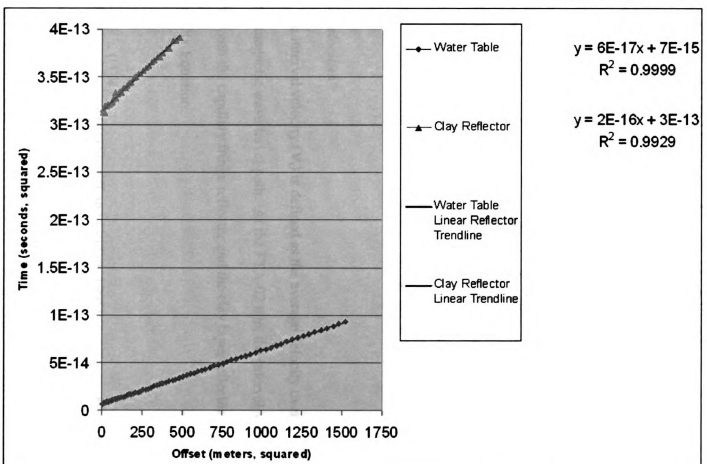

Figure 20. X^2-T^2 analysis for each reflector.

Table 5. Calculated RMS velocities	
Reflector / Material Above Reflector	**RMS Velocity of Material**
Capillary fringe / Unsaturated Zone	1.33×10^8 m/s
Clay layer / Saturated and Unsaturated Zone	7.84×10^7 m/s

analysis method has similar estimated velocity values for the subsurface media.

All assumptions about the subsurface materials, data acquisition methods, and data analysis methods described below are satisfied at the FTA-02 site. Proper antennae coupling with the ground surface was maintained at all times. The selected mutestretch value eliminated data collected from large offsets relative to reflector depths. Also, compiled well-log data, core analyses, and common shot gather analyses all indicate nearly horizontal layering within the shallow subsurface at the FTA-02 site.

Interval Velocities

The interval velocity (V_i) is defined as the average velocity over some interval of the electromagnetic wave travel path. At the FTA-02 site, the interval velocity of the media between the capillary fringe reflector and the clay layer reflector was calculated using the Dix Equation:

$$V_i^2 = \frac{V_n^2 * t_n - V_{n-1}^2 * t_{n-1}}{t_n - t_{n-1}} \quad (4)$$ (Sheriff and Geldart, 1995)

where V_n and t_n are the RMS velocity and zero-offset two-way travel time corresponding to the n^{th} reflector, respectively (Sheriff and Geldart, 1995). The Dix Equation is very

unstable, which has been documented by Sheriff and Geldart, 1995 and Yilmaz, 1987. Slight deviations in RMS velocities often result in exaggerated differences in calculated interval velocities. As a comparison to the interval velocity values obtained from the Dix Equation, a weighted velocity average based on the travel-time within each layer was used to calculate the interval velocity. Table 6 summarizes the interval velocities calculated using each method.

Table 6. Calculated interval velocities.

	Analytical Method	
	Velocity Spectrum (m/sec)	**X^2-T^2 Method (m/sec.)**
Media above capillary fringe (i.e., unsaturated media)	1.353×10^8	1.329×10^8
Interval velocity of saturated media below capillary fringe and above clay layer calculated using Dix Equation	6.70×10^7	6.40×10^7
Interval velocity of saturated media below capillary fringe and above clay layer calculated using weighted average	7.13×10^7	6.87×10^7

An estimated interval velocity value of 6.78×10^7 meters/second for the saturated zone will be used for further data analysis, which is equivalent to the average of the four interval velocity values presented in Table 6. Equation (2) was again used to compare the estimated saturated velocity value with those published in literature. Wet soil typically has a dielectric constant of approximately 25 (Annan, 2001). Therefore, the velocity of an EM wave passing through wet soil is approximately 6×10^7 m/s, which is similar to the value of 6.78×10^7 m/s estimated at the FTA-02 site. Differences between laboratory and site-specific estimates are due to slight differences in the electrical properties of different soil types and the presence of different ions in the groundwater (Annan, 2001).

CONVERTING TIME TO DEPTH IN A GPR TRANSECT

To estimate depths from measured reflection times, an accurate velocity analysis is required. As noted above, accurate velocity calculations were made to properly convert time to depth within the GPR data. The depths equate to EM wave propagation distances, which are necessary in calculating the attenuation of the wave as it passes through the subsurface media. The RMS velocities within the media above the capillary fringe and above the clay layer were calculated using the velocity spectrum analysis and the X^2-T^2 method. The interval velocity, also referred to as the average velocity of the media between two reflectors, was calculated for the media between the capillary fringe and the clay layer. Using these calculated velocity values, the depths to the capillary fringe and clay layer identified at the FTA-02 site were calculated (Table 7).

Table 7. Calculated depths to capillary fringe and clay layer

	Analytical Method	
Depth from Ground Surface	**Velocity Spectrum (m)**	**X^2-T^2 Method (m)**
Depth to Capillary Fringe	5.56	5.58
Depth to Clay Layer (based on two-way travel time to clay reflector and estimated NMO velocity)	22.66	21.91
Depth to Clay Layer (based on depth to capillary fringe + depth to clay using interval velocity)	21.81	21.69

Comparison of Calculated Depths to Measured Depths

Depth-to-water was recorded from the multi-level well network at the FTA-02 site on May 12, 1999, two days prior to completing the GPR survey (Figure 2). No precipitation event occurred between May 12 and 14, 1999. Therefore, the change in the water table elevation during that time is considered negligible. The depth-to-water

(below ground surface) measured in multi-level well ML-9, which is the closest well to the center of the CMP gather, was 5.67 meters. Multi-level well ML-9 is located 36.5 meters southwest of the CMP gather's central location. The location, and ground surface and casing elevations were surveyed for each well, and referenced to NGVD. Therefore, the groundwater elevation at ML-9 is calculated by subtracting the depth-to-water (measured from top of casing) from the surveyed casing elevation. Surveyed ground surface elevations and calculated water table elevations were interpolated between known points along the GPR transect and are shown in Figure 21. Note that the water table elevations were extrapolated to the southwest of MW-10 and to the northeast of ML-9. Since there is no well located at the center of the CMP gather, the extrapolated water table elevation at this location is the best approximation. The error associated with this approximation is minimal because the maximum difference in groundwater elevations measured between any two multi-level wells during this sampling event and located along the GPR transect is 0.27 meters. Subtracting the extrapolated groundwater elevation from the surveyed ground surface elevation at the center of the CMP gather results in a depth-to-water estimate of 5.66 meters. Table 8 lists the differences between the calculated depth to the capillary fringe and the estimated water table depth.

Table 8. Differences between measured and calculated depths to the water table and capillary fringe.

Estimated Depth to Water Table (m)	Calculated Depth to Capillary Fringe Using the Velocity Spectrum (m)	Calculated Depth to Capillary Fringe Using the X^2-T^2 Method (m)
5.66	5.56	5.58
Difference Between Measured and Calculated Depth (m)	0.10	0.08

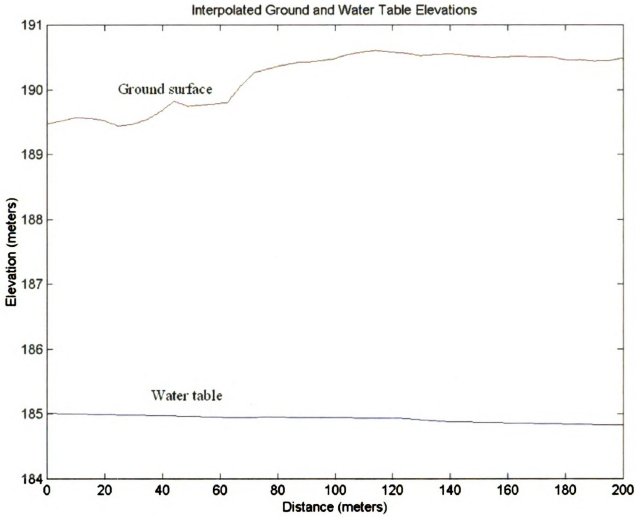

Figure 21. Interpolated ground and water table elevations.

As shown above, each velocity analysis method has calculated the depth-to-water very closely to the estimated value. As previously noted, the electromagnetic wave actually reflects off the top of the capillary fringe resulting in a slight discrepancy (i.e., shallower estimate) between depth to the actual water table and the same depth recorded by GPR (Barber and Morey, 1994). Therefore, the differences between the estimated depth to water table (from extrapolated direct water table measurements) and the calculated depth to the capillary fringe (from GPR data) are expected. Annan and Chua (1992) noted that the water table is a highly gradational boundary encountered by an electromagnetic wave. Capillary action can smear the water distribution between the unsaturated and saturated zones as a function of grain sizes (Annan and Chua, 1992). The typical capillary rise observed in medium to coarse sands, which are present at the site, is 0.25 to 0.15 meters, respectively (Fetter, 1994). These capillary rise estimates are very close to the differences between the estimated depth to water table and the calculated depth to the capillary fringe listed above.

The clay layer identified in the GPR transect at the FTA-02 site ranges from 24.4 meters below grade in the northern part of the former Wurtsmith Air Force base to 9.1 meters below grade at the west edge of the former base, with an average depth of 19.8 meters below grade. In general, the deepest occurrences of the clay layer are in the northeast portion of the former base (Stark *et. al.*, 1983; Nash *et. al.*, 1997). The exact depth to the clay layer has not been measured at the location of the GPR transect and CMP gather. However, calculating the difference between the ground elevation (Figure 22) and the clay surface elevation (Figure 23) in the southwest portion of the former WAFB at the FTA-02 site estimates the depth to clay as approximately 19.81 meters (65

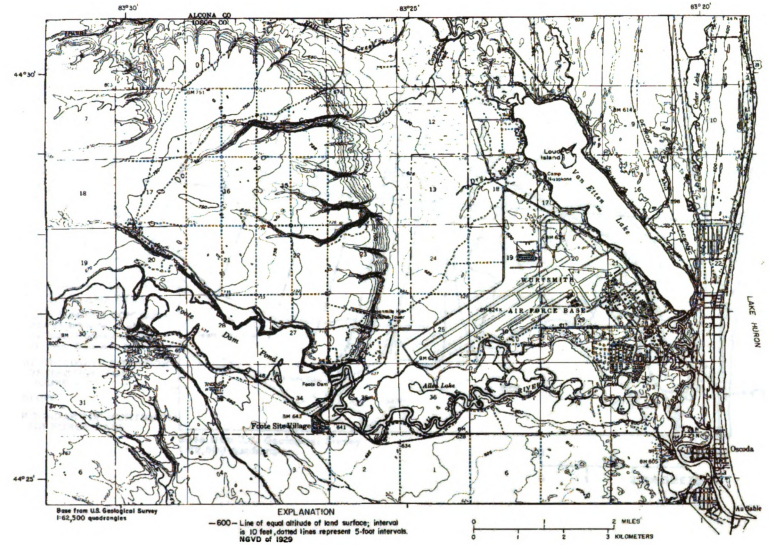

Figure 22. Ground elevations (ft.) at former Wurtsmith Air Force base (Stark, Cummings, and Twenter, 1983).

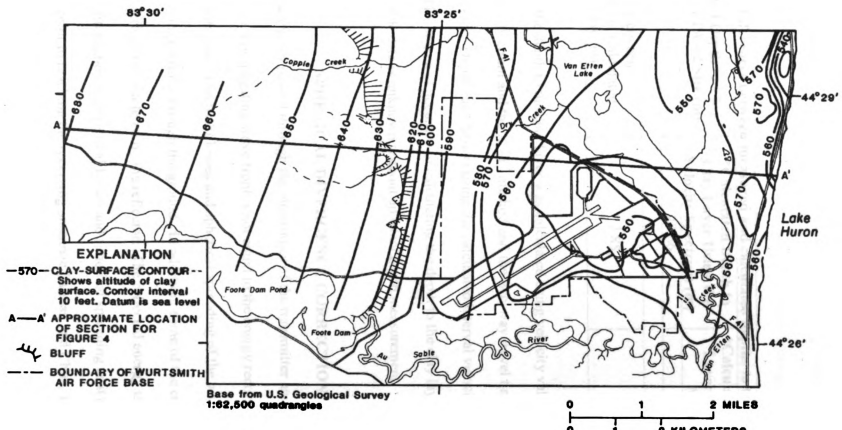

Figure 23. Clay surface elevations (ft.) at former Wurtsmith Air Force base (Cummings and Twenter, 1986).

feet). Table 9 lists the differences between calculated and estimated depths to the clay layer.

Table 9. Differences between measured and calculated depths to the clay layer.		
Estimated Depth to Clay Layer at FTA-02 Site (m)	***Calculated Depth to Clay Layer Using the Velocity Spectrum (m)**	***Calculated Depth to Clay Layer Using the X^2-T^2 Method (m)**
19.81	22.66	21.91
Difference Between Estimated and Calculated Depths to Clay (m)	*2.85	*2.10

*Note that the depth to the clay layer was calculated using velocity values obtained from the velocity spectrum and the X^2-T^2 method and the two-way travel time from the surface to the reflector. Depth calculations using the calculated interval velocities were very similar. The degree of accuracy to calculating the depth to the clay layer from the acquired GPR data is unknown without an exact depth measurement.

SPHERICAL DIVERGENCE CORRECTION

The energy passed through the electronics of the transmitter and induced into the subsurface as a propagating wave front is not equal to the energy recorded in the receiving antennae. Electrical losses and spherical spreading of the wave front attenuate the energy propagating through the ground. In addition, some of the energy that reaches the target reflector is scattered by the reflector. The reflected energy is once again subject to attenuation by electrical losses and spherical spreading as it propagates through the media prior to reaching the receiving antennae (Annan and Chua, 1992). As such, in order to quantify the amount of attenuation an EM wave experiences due to electrical

losses as it propagates through the subsurface media, which is a function of the conductivity of the media, energy loss from spherical spreading must also be quantified.

The wave field generated by the transmitting antennae is conceptually thought of as a point source that generates a spherical wave field. As the spherical wave field spreads outward from the point source in a homogeneous media, the energy density decays proportionately to $(1/r^2)$, where r is the radius of the wave front, which corresponds directly to the propagation depth of the wave (Yilmaz, 1987). As such, a time-variant gain was applied to the filtered GPR transect data to correct for spherical divergence. Amplitude is proportional to the square root of the energy. Therefore, the recorded energy at each point within the transect was multiplied by its corresponding depth (depth calculation discussed above). The GPR transect corrected for spherical divergence is shown in Figure 24 (see Appendix). The spherical divergence correction resulted in a GPR data set with slightly enhanced reflection amplitudes at depth. The gain applied to the GPR data is relatively small due to the shallow features at the site.

AMPLITUDE AND ATTENUATION ANALYSIS

The novel approach to quantitatively assessing the attenuation of the transmitted GPR signal and subsequently calculating the specific conductivity of the groundwater is to analyze amplitude changes with distance. As mentioned above, previous studies by others have not analyzed GPR data to quantitatively assess hydrogeologic and geochemical properties of groundwater. Instead, GPR has been used to simply image and/or delineate plume geometries. Researchers have established typical attenuation values for a range of common materials by using empirical relationships between the

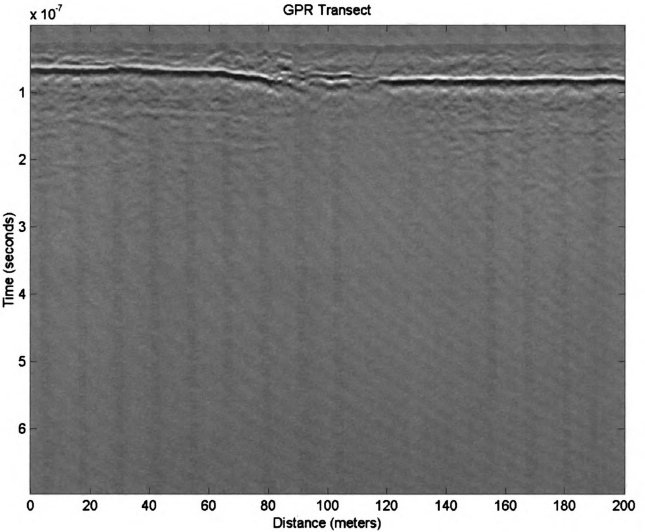

Figure 24. GPR transect at FTA-02 site with gain applied to correct for spherical divergence.

electrical properties of the materials and EM waves (Sensors & Software, 1996). However, these typical attenuation values are not useful when a complex contaminated system is encountered and many of the factors contributing to attenuation may be unknown. As such, an approach has been developed to quantify the amount of attenuation directly from the GPR data.

The decrease in amplitude of a propagating EM wave front in rocks and sediments due to attenuation (i.e., absorption of the wave front by electrically conductive materials) is exponential with distance and can be represented as:

$A = A_0 e^{-\alpha x}$ (5) (Sheriff and Geldart, 1995)

where A is the amplitude of the initial wave front, A_o, after traveling a fixed distance, x and experiencing attenuation coefficient, a (Sheriff and Geldart, 1995). By measuring the reduction in amplitude of the transmitted GPR signal, the attenuation coefficient (a) of the shallow aquifer material at the FTA-02 site was quantified.

The decrease in amplitude between the water table and clay layer reflections observed at the FTA-02 site was analyzed to quantify the amount of attenuation. Figure 25 shows the amplitudes of the water table and clay layer reflections. This method of calculating attenuation as a function of distance has the advantage of utilizing well-defined reflection events that are easily identified and analyzed in the GPR data set. However, this method is limited to conditions where reflectors are identified and does not include amplitude reduction independent of reflection amplitudes, which may have resulted in the boundary effects discussed below.

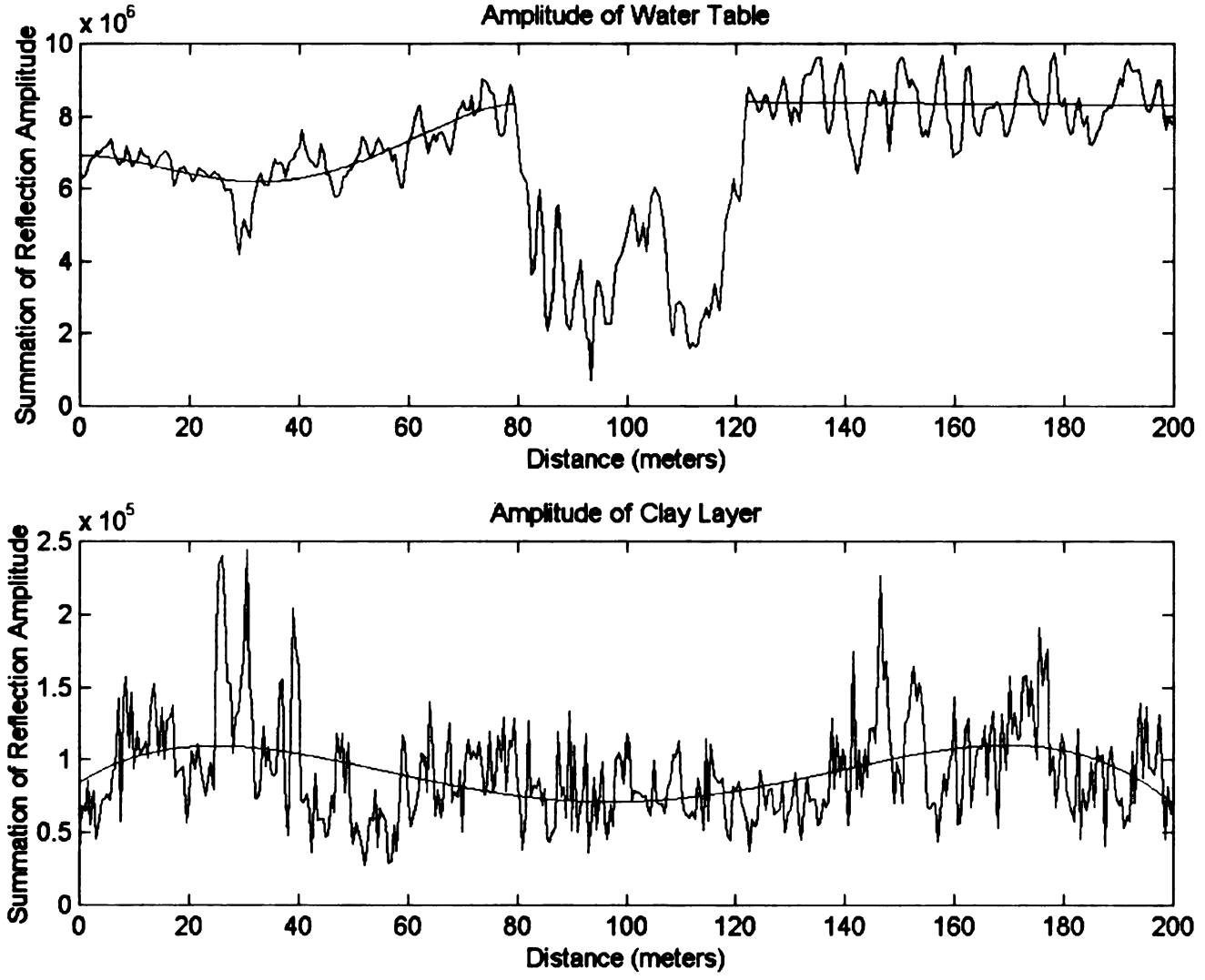

Figure 25. Amplitudes of water table and clay layer reflections.

The amplitude of each reflection was calculated by summing the absolute amplitude values along one complete wavelength of the reflected signal (see Appendix). The amplitude of each reflection was also calculated using the maximum absolute amplitude value along one complete wavelength of the reflected signal. The relative reflection amplitudes differ depending on the calculation method, but the energy loss (i.e., attenuation) between reflections is nearly identical. Therefore, it is believed that either method can be used. Also note that the amplitude of the water table reflection is significantly reduced between approximately 160-meters and 244-meters within the GPR transect, which corresponds to the location of the identified groundwater contaminant plume. This observation recorded in the GPR data may be caused by the presence of light non-aqueous phase liquid (LNAPL) contaminants on the water table surface and/or a significant concentration of residual and/or vapor phase contaminants within the vadose zone. These conditions do not meet the assumptions of the model presented herein. Therefore, the amplitude of the water table reflection between approximately 160-meters and 244-meters within the GPR transect will not be used to quantify the attenuation.

Trend lines were fit to the water table and clay layer amplitude curves (Figure 25). The trend lines smooth slight amplitude differences between each GPR trace that may have been caused by differences in antennae coupling and incident angles. Trend lines were fit to the western and eastern portions of the water table amplitude curve, excluding the area between 160-meters and 244-meters within the GPR transect (Figure 25). The trend lines for the clay layer amplitude curve and the western portion of the water table amplitude curve were best fit using a fourth-order polynomial. The trend line

for the eastern portion of the water table amplitude curve was best-fit using a first-order polynomial (see Appendix).

By solving the exponential decay relationship presented in Equation 5 for a, the attenuation of the EM wave front is defined as:

$$\alpha = \frac{\ln(\frac{A}{A_0})}{-x} \quad (6)$$

Therefore, the attenuation of the EM wave front within each GPR trace between the water table (A_0 , trend line) and clay layer (A , trend line) reflections are quantified using Equation 6. The distance (x) is calculated from the GPR data as one half the difference in two-way travel times between the water table and the clay layer, multiplied by the velocity of the saturated media (see Appendix; Figure 26).

As shown in Figure 26, the increased attenuation values near the western and more notably eastern ends of the GPR transect appears to be an artifact of the best-fit trend line for the clay layer reflection amplitude curve and apparent reduced clay layer reflection amplitudes. The trend line is a function of a fourth-order polynomial and decreases in value near the western and eastern edges of the GPR transect. As such, the calculated attenuation values in these areas have been artificially elevated. The reductions in clay layer reflection amplitudes in the western and eastern portion of the transect were unexpected and the cause is unknown. A different method of analyzing amplitude loss may be required to improve the attenuation quantification in these areas.

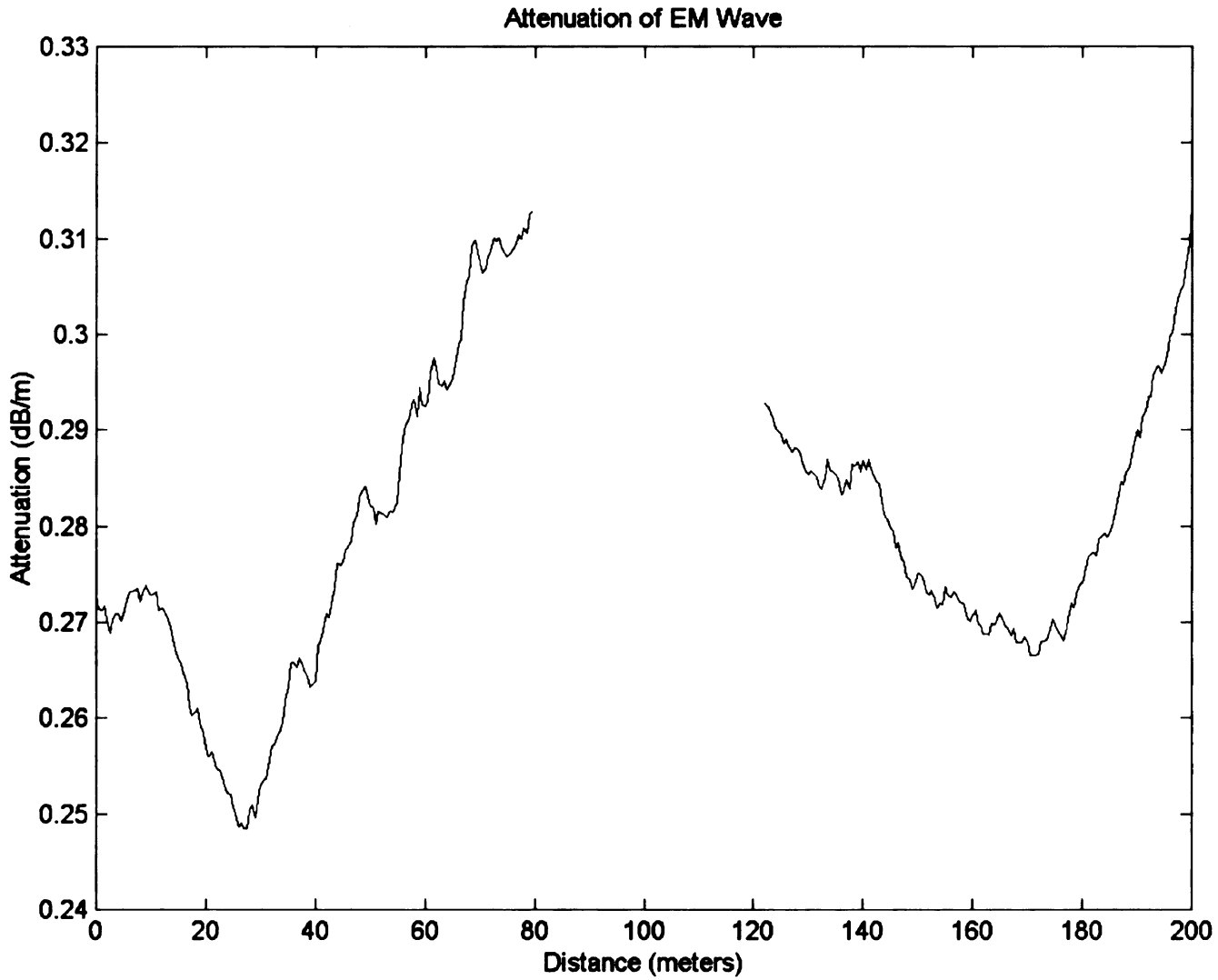

Figure 26. Attenuation of EM wave front.

SPECIFIC CONDUCTIVITY CALCULATION

Elevated specific conductivity was measured in groundwater samples collected within the contaminant plume (discussed later and detailed in Table 10) and, as previously discussed, a 'shadow zone' was observed in a GPR transect through the plume. The 'shadow zone' is caused by EM wave attenuation, which can be calculated from the GPR data within each trace of the GPR transect. As described below, empirical relationships between attenuation and conductivity parameters enable the calculation of the specific conductivity of the groundwater at the FTA-02 site.

Gueguen and Palciauskus, 1994 indicated that the properties of an electromagnetic wave can be described by using solutions to Maxwell's equations in three dimensions. However, these solutions are mathematically very complex. Therefore, to investigate the important features of the electromagnetic wave, they simplified the mathematics by applying the solution for a harmonic plane wave to Maxwell's Equations for electromagnetic waves. This is a well recognized and standard approximation for analyzing electromagnetic waves. The results define the equation for the electromagnetic wave propagation and attenuation in a medium, such that:

$$k = \sqrt{(\varepsilon\mu\omega^2 + i\omega\sigma)} = k_{real} + ik_{imaginary} \quad (7)$$ (Gueguen and Palciauskus, 1994)

where k is the complex wave number, e is the electrical permitivity (Farads/meter), μ is the magnetic permeability (Newton/Ampere^2), ? is the angular frequency (MHz), and s is the conductivity of the media (Siemens/meter). The real part of k describes the

propagation of the electric field and the imaginary part of *k* describes the amount of attenuation with distance. The imaginary part of *k*, or attenuation (α) is defined as:

$$\alpha = \omega * \sqrt{\frac{\varepsilon\mu}{2}} * \sqrt{\sqrt{1+(\frac{\sigma}{\varepsilon\omega})^2} - 1} \quad (8)$$ (Gueguen and Palciauskus, 1994)

The attenuation of the EM wave is therefore a function of conductivity and other electrical properties of the media. As described above, the attenuation of the wave can be calculated from the GPR data by evaluating the exponential decay of reflection amplitudes. The direct relationship between attenuation and conductivity can be evaluated as the derivative of Equation 8 with respect to σ:

$$\frac{\partial\alpha}{\partial\sigma} = \frac{\sqrt{\sigma * \frac{\varepsilon\mu}{2}}}{\sqrt{\sqrt{1+(\frac{\sigma}{\varepsilon\omega})^2} - 1} * \sqrt{1+(\frac{\sigma}{\varepsilon\omega})^2}} \quad (9)$$

If we assume that changes in conductivity are greater than any other changes in the x-dimension and are the only cause of differing amounts of attenuation, then the following relationships are also true:

$$\frac{\partial\alpha}{\partial\sigma} \approx \frac{\Delta\alpha}{\Delta\sigma} \quad (10)$$

$$\sigma_n \approx \sigma_{n-1} + \frac{\Delta\alpha}{\partial\alpha/\partial\sigma} \quad (11)$$

where n is the individual trace number within the GPR transect. As such, the change in conductivity ($\Delta\ \sigma$) of the media within each GPR trace can be calculated using the change in attenuation ($\Delta\ \alpha$) between traces and the derivative of the equation that defines the attenuation ($\partial\ \alpha / \partial\ \sigma$). $\Delta\ \alpha$ between individual traces within the GPR transect can be calculated directly from the attenuation values shown in Figure 26. $\Delta\ \sigma$ is calculated using the relationships above. However, an initial conductivity value is required to calculate $\Delta\ \sigma$. The initial conductivity value used for the western end of the transect is 180 micro-Siemens/centimeter, which is equal to the background specific conductivity values measured by others at the site (Bermejo *et. al.*, 1997; Nash *et. al.*, 1997; Sauck *et. al.*, 1998; Sauck, 2000) and approximately equal to the average specific conductivity value of 188 micro-Siemens/meter measured at four depths within multi-level well ML-10.

The conductivity calculated from the relationships presented above should be referred to as the effective conductivity (σ_{eff}) because the propagating EM wave front is subject to absorptive losses from the conductivity of both the sediment grains and the pore waters. Because there is such a high contrast between the conductivity of the silicate sediments ($\sigma_s \approx 10^{-14}$ to 10^{-10} Siemens/meter) and ion-rich fresh water solutions occupying the pore volumes ($\sigma_w \approx 10^{-1}$ to 1 Siemens/meter), it is understood that most electrical currents flow through the pore waters. Therefore, the effective conductivity of saturated sediments is equal to the specific conductivity of the fluid (σ_w) reduced by a

formation factor (F), which is dependent on pore-size parameters, including porosity (F) and tortuosity:

$\sigma_{eff} = \frac{\sigma_w}{F}$ (12), (Gueguen and Palciauskus, 1994).

The microstructure details required to directly calculate the formation factor are not known for the sediments at the FTA-02 site. As such, Archie's Law was used to determine the relationship between the formation factor and porosity. Archie's Law defines the formation factor as:

$F = \phi^{-m}$ (13), (Gueguen and Palciauskus, 1994)

where m is referred to as a cementation factor, which increases as tortuosity of the pore volumes increases (Backe *et. al.*, 2001). As mentioned above, the approximate porosity (F) of the sediments is 0.3, which falls within the range of typical porosity values for unconsolidated sand deposits (Freeze and Cherry, 1979) and can be expected of glacial deposits with various grain sizes including lacustrine sediments, ice-contact sediments, and alluvium present at the FTA-02 site. A typical range of values for the cementation factor for unconsolidated quartz sand is 1.3 to 1.5 (Backe *et. al.*, 2001; Bigalke, 2000; Boving and Grathwohl, 2001; Fitterman and Deszcz-Pan, 2001; Hwang *et. al.*, 2004; Kwader, 1986) and a typical range of values for the cementation factor for geologic materials is 1.5 to 2.5 (Gueguen and Palciauskus, 1994). However, no universal cementation factor exists for individual sand types because *m* can vary simply by the

orientation and shape of the pores (Boving and Grathwohl, 2001). In addition, modeling by others has calculated a cementation factor of 3.2 in unconsolidated sands (Backe *et. al.*, 2001). The model results for the calculated groundwater specific conductivities were calibrated to a weighted average of the measured groundwater specific conductivities, described below, using a formation factor of approximately 16.9. Therefore, according to Archie's Law and if we assume a porosity of 30%, the cementation factor is equal to 2.35 and the effective conductivity of the media and background waters at the FTA-02 site is equal to approximately 10.6 micro-Siemens/centimeter. A cementation factor of 2.35 is slightly higher than values typically used for unconsolidated quartz sands. However, 2.35 is a realistic value for typical geologic materials. In addition, the varying redox environments within the contaminant plume may facilitate the production of various coatings on the individual sand grains, such as metal-sulfides and/or biomass from the active microbial communities. These materials would result in decreased pore volumes, increased tortuosity, and increased cementation factors.

It is important to note that the site specific porosity and cementation factor have not been independently quantified for the FTA-02 site. Therefore, according to Archie's Law, there are an infinite number of porosity and cementation factor combinations that can result in a formation factor of 16.9. The relationship is highly sensitive to changes in the cementation factor. If porosity is as low as 15% then the cementation factor required to maintain the same formation factor is approximately 1.5. The model is calibrated using a formation factor of approximately 16.9 and additional research is required to quantify the site specific porosity and cementation factor.

The calculated specific conductivity of the groundwater at the FTA-02 site is shown in Figure 27 (see Appendix). The highest electrically conductive groundwater is located near the center of the GPR transect, which directly corresponds to the location of the contaminant plume. Once again, the increased specific conductivity values calculated near the western and, more notably, eastern ends of the GPR transect appear to be an artifact of low clay layer reflection amplitudes in these areas. Therefore, the calculated attenuation in these areas is over-estimated because there is no suspected contamination there.

The attenuation along each GPR trace is calculated from the water table reflection to the clay layer reflection, and represents the total attenuation encountered within the saturated media above the clay layer. As such, the estimated groundwater specific conductivity values shown in Figure 27 are representative of the average specific conductivity values along each trace of the GPR transect within the saturated media above the clay layer. Therefore, the calculated specific conductivity values were calibrated (by adjusting the formation factor, as discussed above) to a weighted average of the measured specific conductivity values (Figure 28, Table 10).

The model for calculating the specific conductivity of groundwater using GPR has been calibrated to the direct measurements recorded within multi-level wells ML-3, ML-4, ML-5, ML-7, ML-8, ML-9, and ML-10 at the FTA-02 site between June 5 and June 10, 2000, which are shown as asterisks on Figure 29. The values measured at each sampling depth within each multi-level well have been averaged using a weighted average to represent the composite groundwater the EM wave front passed through in the GPR transect. The weighted averages were calculated based on depths defined by the

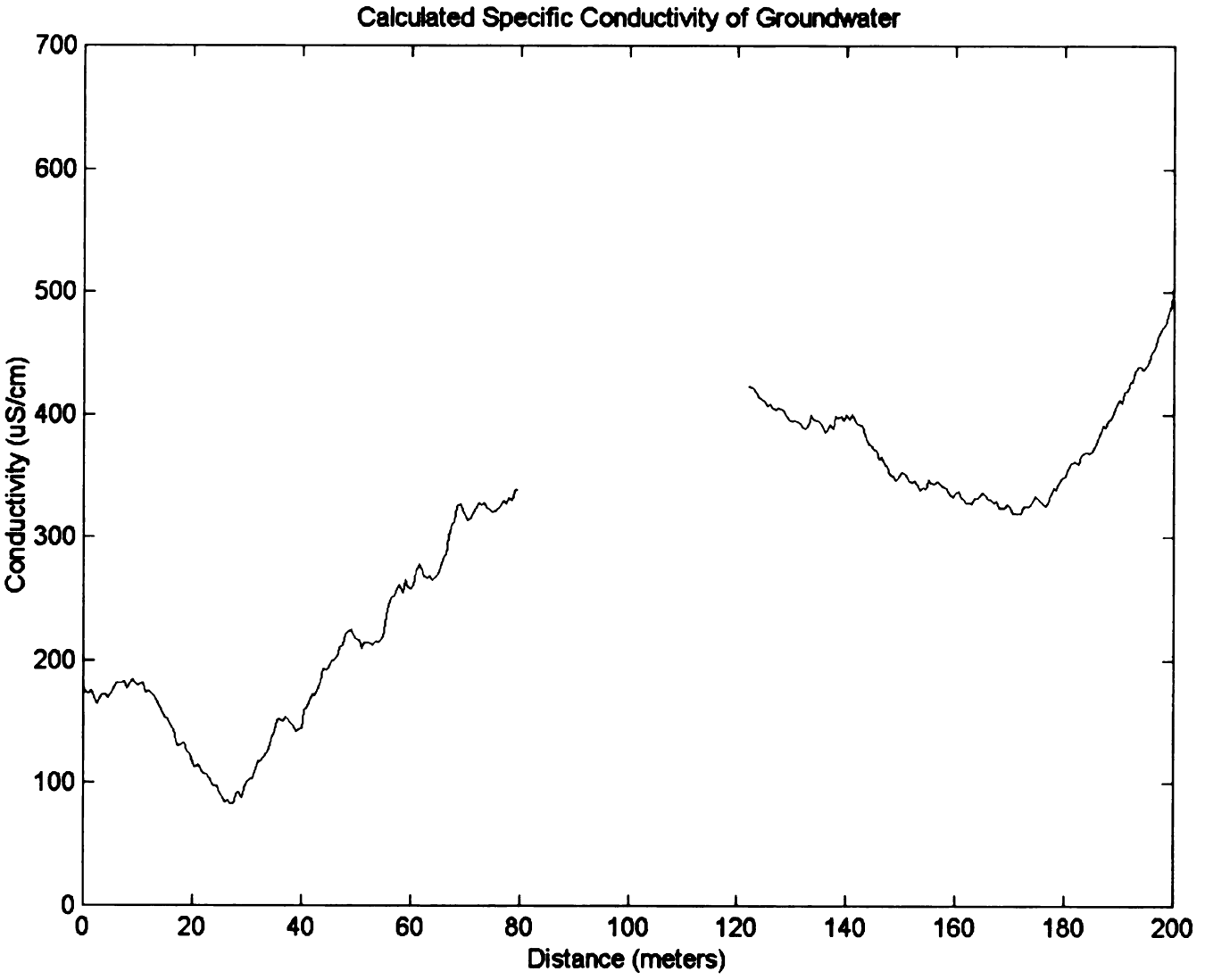

Figure 27 Calculated specific conductivity of groundwater.

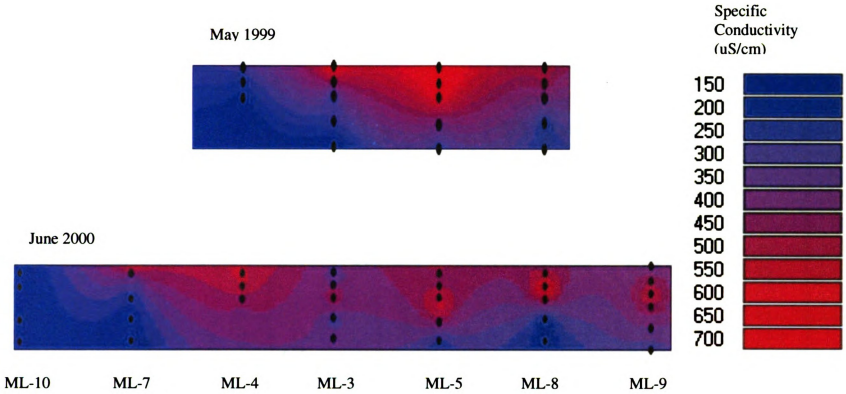

Figure 28. Interpolated groundwater specific conductivity values.

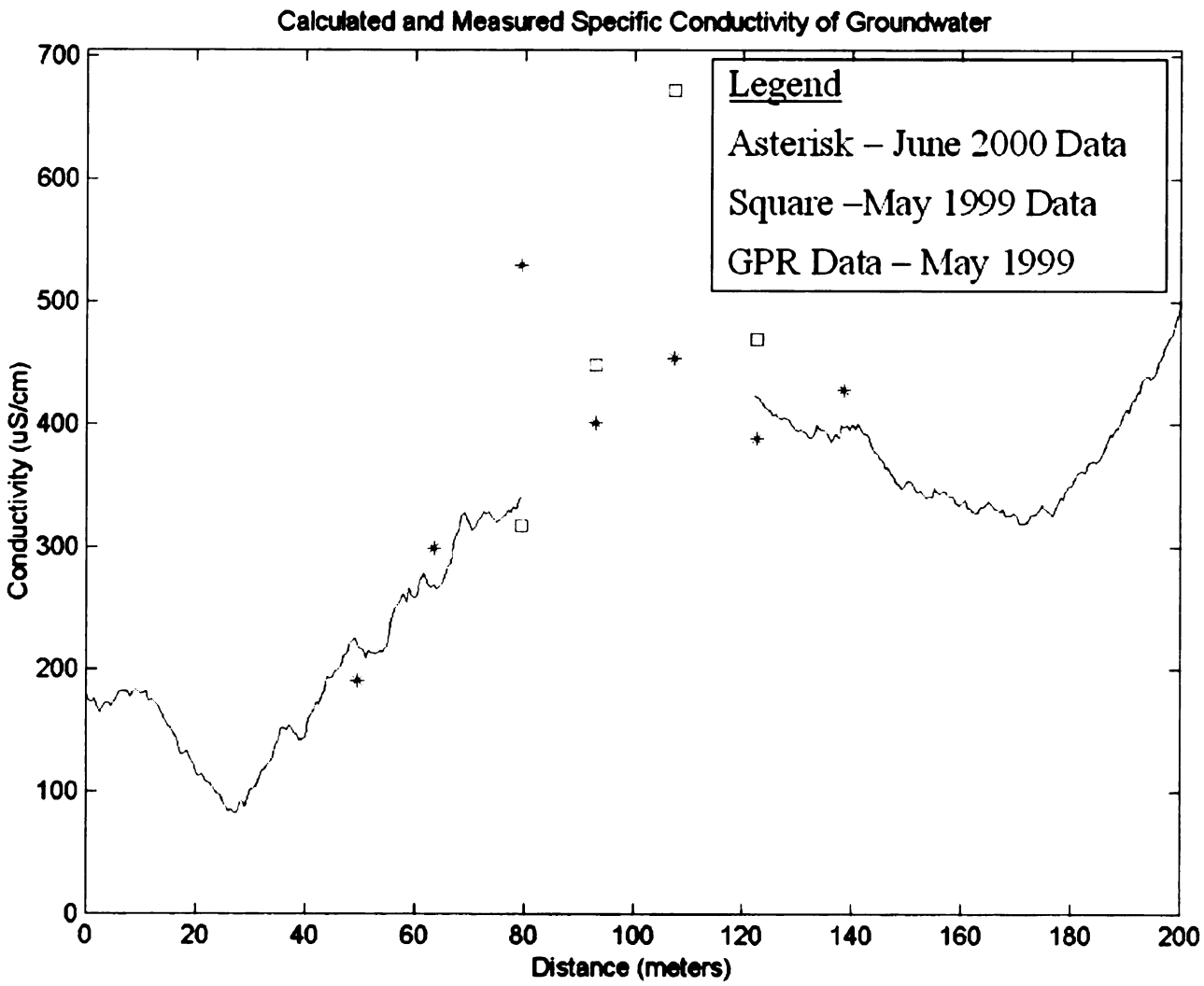

Figure 29. Calculated and measured specific conductivity of groundwater.

water table elevation and the midpoints between sample depths. The GPR data used to create the model presented herein was collected approximately one year earlier in May 1999. However, groundwater specific conductivity was only measured in wells ML-3, ML-4, ML-5, and ML-8 in 1999 (Figure 28). The June 5 to June 10, 2000 data set of measured specific conductivity values is the most comprehensive data set for the site. The measured values from each sampling event are similar, with the exceptions of ML-4 and ML-5, as shown in Table 10.

Table 10. Weighted Average of Measured specific conductivity values.

Well	Specific Conductivity (uS/cm, May 1999)	Specific Conductivity (uS/cm, June 2000)
ML-3	447.6	400.4
ML-4	316.7	530.0
ML-5	672.5	453.2
ML-7	Not Measured	298.4
ML-8	469.5	388.1
ML-9	Not Measured	427.3
ML-10	Not Measured	190.7

The measured specific conductivity of the groundwater was more variable amongst the multi-level wells in 1999 than in 2000. This may be the result of slightly drier conditions in 1999. Water table elevations measured in the multi-levels wells on a nearly bi-monthly basis were approximately 0.8 meters lower in 1999 than in 2000, and the sampling event followed a 3-month period of low precipitation and declining water table elevations. The drier conditions may have resulted in areas of differential biodegradation and resultant specific conductivity measurements. In contrast, the 2000 sampling event occurred after a 4-month increase in water table elevations, indicative of greater

precipitation volumes. The increased precipitation may have leached ions into the groundwater and created a slightly more homogeneous contaminant plume with regards to specific conductivity measurements.

CONCLUSIONS

The research presented herein provides a new mechanism to evaluate the nature and extent of groundwater contamination using high-resolution GPR methods from the ground surface. The sequence of data processing techniques produced a calibrated site-specific model that quantitatively evaluates the specific conductivity of groundwater within a contaminant plume. The model is based on data from the study site and documented investigations at other sites that show contaminant plumes with well established microbial activities and undergoing biodegradation will exhibit groundwater with elevated specific conductivities as a result of ions leaching from the sediments. This differs from contaminant plumes that have not undergone significant biodegradation and/or have LNAPL at the water table, which is highly resistive and enhances GPR reflections. The increased groundwater specific conductivity identified on-site is also the result of increased sodium mass discharged from a bioreactor as part of a pilot-scale pump-and-treat system installed at the study site. The model increases the usefulness of GPR from simply a tool used to image and delineate a contaminant plume to a non-intrusive tool for estimating the specific conductivity of groundwater.

By altering the site-specific parameters, the model can be used on a number of sites, given general knowledge of the aquifer parameters, sufficient GPR signal penetration, and limited naturally occurring conductive materials such as clays and

naturally conductive groundwater. The model enables the user to quickly and accurately evaluate a specific aspect of the groundwater quality (i.e., specific conductivity) without installing monitoring wells and collecting groundwater samples for laboratory analysis. The presence of elevated groundwater specific conductivity values above background, as calculated by the model presented above, is consistent with the location of groundwater contaminant plumes.

APPENDIX

APPENDIX. MATLAB® CODES

```
%%%%%%%%%%%%%%%%%%%%%%%%%%%%%%%%%%%%%%%%%%%%%
% 200 m long shot gather along PZ2 transect line
% WSPZD = raw data
% WSPZD1 = raw data with first arrival at zero
% WSPZfiltx = dewowed data
% WSPZagx = AGC gain on data
fid=fopen('WSPZ1_50.SGY','r','l');
[WSPZD,H]=readsegy(fid);
fclose(fid);
WSPZdt=H(1).dt*1e-12;
[WSPZnt,WSPZnx]=size(WSPZD);

%%%%%%%%%%%%%%%%%%%%%%%%%%%%%%%%%%%%%%%%%%%%%
%Removal of bad traces
btr1=(WSPZD(:,256)+WSPZD(:,258))/2;
WSPZD=[(WSPZD(:,1:256)) btr1 (WSPZD(:,258:WSPZnx))];

%%%%%%%%%%%%%%%%%%%%%%%%%%%%%%%%%%%%%%%%%%%%%
%Set data to time zero. Time zero is obtained from *.hd file
WSPZD1=WSPZD(44:WSPZnt,:);
[WSPZnt1,WSPZnx]=size(WSPZD1);
WSPZt1=(1:WSPZnt1)*WSPZdt;
WSPZx1=(0:0.5:(WSPZnx*0.5));

%%%%%%%%%%%%%%%%%%%%%%%%%%%%%%%%%%%%%%%%%%%%%
%Frequency Spectrum
trace=WSPZD1(:,1);
subplot(2,1,1), plot(WSPZt1,trace), axis([-0.5e-7 5e-7 -4e4 4e4])
title('First trace from GPR transect'), xlabel('Time(s)')
freq_spec=(fft(trace)).*(conj(fft(trace)));%Frequency Spectrum
df=1/(length(WSPZt1)*WSPZdt);%Delta frequency for x-axis
N=df*length(WSPZt1);
freq=0:df:N-1;
subplot(2,1,2), plot(freq,freq_spec)
axis([0 5.5e8 -0.5e11 5.5e11])
title('Power spectrum'), xlabel('Frequency (Hz)')
%%%%%%%%%%%%%%%%%%%%%%%%%%%%%%%%%%%%%%%%%%%%%
%Filter data

function filtx=bandpass(xx,dt,flow,fhigh,n,ps)
%%%%%%%%%%%%%%%%%%%%%%%%%%%%%%%%%%%%%%%%%%%%%
% function filtx=bandpass(xx,dt,flow,fhigh,n,ps)
%
% This function filters an array of data xx
% with sampling rate of dt with a bandpass filter
% xx-data size[nt,nx]
```

```
% flow- lowfrequency (min frequency, Hz)
% fhigh- high frequency (max frequency, Hz)
% n - number of points in filter (optional input)
% ps- phase=0 for zero phase input, (optional input)
% the filter coeficients are calculated with fir1,
% with n point filter. default n=128, if n not specified on input.
% The filtering is done with fftfilt, this introduces a delay as it
% is not a zero-phase filter. delay is ~ 0.5*n time points. for zero phase
% filter insert the optional parameter ps=0.

% Written by Ran Bachrach
%%%%%%%%%%%%%%%%%%%%%%%%%%%%%%%%%%%%%%%%%%%%%%%%%%%%%%%%%%%%%%%%%%%%%%%%%%%

[nt,nx]=size(xx);
if nargin<5, n=128; end;
if nargin<6  ps=1; end;
fN=0.5/dt; %nyquist frequency
f1=flow/fN;
f2=fhigh/fN;
df=1/(dt*nt);
B=fir1(n,[f1,f2]);
if ps==1
filtx=fftfilt(B,xx); %introduces linear phase delay
elseif ps==0
 filtx=filtfilt(B,1,xx); %zero phase filter
end

%%%%%%%%%%%%%%%%%%%%%%%%%%%%%%%%%%%%%%%%%%%%%%%%%%%%%%%%%%%%%%%%%%%%%%%%%%%
WSPZfiltx=bandpass(WSPZD1,WSPZdt,19e6,250e6,128,0);
%%%%%%%%%%%%%%%%%%%%%%%%%%%%%%%%%%%%%%%%%%%%%%%%%%%%%%%%%%%%%%%%%%%%%%%%%%%

%Apply AGC to data
function agx=agc(xx,t,dt,opt);
% function agx=AGC(xx,t,dt,opt);
% This function calculates the smooth AGC display of the data.
% xx - data matrix size(nt,nx) (Can be shot gather or cdp or just one trace)
% t  - time length of the agc operator
% dt - sampling rate, or t=#of samples to be averaged dt=1.
% opt- normalization option.  opt=2 gives RMS; opt=1 normalize by sum of abs values. Defualt
is RMS
%
% see Yilmaz for details.
%%%%%%%%%%%%%%%%%%%%%%%%%%%%%%%%%%%%%%%%%%%%%%%%%%%%%%%%%%%%%%%%%%%%%%%%%%%
%Written by R. Bachrach
%Modified by T. Mukerji

if nargin==3 opt=2; end
ng=fix(t/dt);
[nt,ny]=size(xx);
for i=1:fix((nt/ng))
  v=[ng*(i-1)+1:ng*i];
```

```
 if opt==2
  M(i,:)=sqrt((sum(xx(v,:).^2))/ng);
  elseif opt==1
  M(i,:)=(sum(abs(xx(v,:))))/ng;
 end
end
x1=[1; [ng/2:ng:ng*fix(nt/ng)]'; nt]; M1=[M(1,:); M; M(end,:)]; xI=[1:nt]';
MI=interp1(x1,M1,xI);
agx=xx./MI;

%%%%%%%%%%%%%%%%%%%%%%%%%%%%%%%%%%%%%%%%%%%%%%%%%%%%%%%%%%%%%%%%%%%%%%%%
WSPZagx=agc(WSPZfiltx,12,WSPZdt);

%%%%%%%%%%%%%%%%%%%%%%%%%%%%%%%%%%%%%%%%%%%%%%%%%%%%%%%%%%%%%%%%%%%%%%%%
%Velocity Analysis

function
[spectrum,vel,Vstk,tstk,Vdix,v,lyrthk]=velocityspectrum2(agx,offset,t1,dt,vmin,vmax,dv,mutestr
ch)
% function
[spectrum,vel,Vdix,v,lyrthk]=velocityspectrum2(agx,offset,t1,dt,vmin,vmax,dv,mutestrch);
%
%  velocityspectrum calculates the velocity spectrum of a CDP gather
%  It uses NMO for calculating constant velocity NMO
%  Then, the user picks the velocity function using interactive mode.
%  Also uses t2dvf to convert the velocity function to depth
%
%  spectrum - Velocity spectrum pannel
%  vel - axis of velocity: vmin:dv:vmax
%  Vdix - interval velocities
%  v - velocity vector (length(t1))
%  lyrthk - thickness(m) of layers differentiated by velocities.
%    vector size is dependent on the number of velocities selected
%    during formation of the velocity spectrum
%  agx- CDP gather (size [nt,nx])
%  offset- distance vector of antenna offset (size ([1,nx]))
%  t1- time vector (size ([nt,1]))
%  dt-  sampling interval
%  vmin,vmax,dv- velocity values for NMO input
%  mutestrch- optional parameter for strech mute. Default = 35%
% see NMO for further details

% written by John MossJuly 21, 2000
% Modified by Ran Bachrach July 25, 2000
%%%%%%%%%%%%%%%%%%%%%%%%%%%%%%%%%%%%%%%%%%%%%%%%%%%%%%%%%%%%%%%%%%%%%%%%
if nargin<8;mutestrch=35;end;
temp=2;  %used later for 'while' statement
[nt,nx]=size(agx);
%%%%%%%%%%%%%%%%%%%%%%%%%%%%%%%%%%%%%%%%%%%%%%%%%%%%%%%%%%%%%%%%%%%%%%%%
figure(1), subplot(1,2,1), imagesc(offset,t1,agx)
```

```
inpopt=questdlg('Would you like to remove data to preserve small
offsets?','velocityspectrum','No');
switch inpopt
   case 'Yes'
defans={'10'}; prompt={'Select x-intercept (integer).'};
dlgtitle='Velocityspectrum';
answer=inputdlg(prompt,dlgtitle,1,defans);
xint=str2num(answer{1});
%Create line that truncates agx to preserve small offsets
line=offset.*(max(t1)/xint);
for j=1:length(offset);
  if offset(j)==xint;
    temp=j;
  end
end
slope=(max(t1)-t1(1))/(temp-1);
line=1:temp;
line(1)=t1(1);
for j=2:temp;
  line(j)=t1(1)+(slope*(j-1));
end
subplot(1,2,1),hold on,plot(offset(1:length(line)),line,'r')
%%%%%%%%%%%%%%%%%%%%%%%%%%%%%%%%%%%%%%%%%%%%%%%%%%%%%%%%%%%%%%%%%%%%%%%%%%%%%%%%
%Creates new agx data set with large offset data deleted
for i=1:length(line);
     for j=1:length(t1);
     if offset(i)>xint;
       agx(:,i)=0;
     end
     if t1(j)<line(i);
       agx(j,i)=0;
     end
  end
end
if length(line)<length(offset); %if xintercept<max offset, length of line < length offset
  temp=length(offset)-length(line);
  for j=1:temp;
    agx(:,nx-j+1)=0;
  end
end
%%%%%%%%%%%%%%%%%%%%%%%%%%%%%%%%%%%%%%%%%%%%%%%%%%%%%%%%%%%%%%%%%%%%%%%%%%%%%%%%
subplot(1,2,2),imagesc(offset,t1,agx)
case 'No',end
%%%%%%%%%%%%%%%%%%%%%%%%%%%%%%%%%%%%%%%%%%%%%%%%%%%%%%%%%%%%%%%%%%%%%%%%%%%%%%%%
vel=vmin:dv:vmax;nv=length(vel);
[nt,nx]=size(agx);spectrum=zeros(nt,nv);
for j=1:nv;
[ZZ]=NMO(agx,offset,0,dt,vel(j),0,mutestrch);

%%%%%%%%%%%%%%%%%%%%%%%%%%%%%%%%%%%%%%%%%%%%%%%%%%%%%%%%%%%%%%%%%%%%%%%%%%%%%%%%
function [ZZ] =NMO(Tr,offset,t0,dt,v,flag,strch);
```

```
%function [ZZ] =NMO(Tr,offset,t0,dt,v,flag,strch);
%
% Input Tr: data to NMO (if flag=0) or spray (if flag=1);
%      [nt,nx]=size(Tr)
%      v: velocity scalar for constant velocity NMO
%      or vector(size [1:nt]') for vriable velocity NMO .
%      offset: Vector with offset values.  size [1:nx].
% t0- two way travel time till 1st live point (use 0 if no delay)
%
%      dt: sampling rate
%      flag to NMO correct=0 (flatten hyperbula)
%      flag to spray (or un-NMO) =1
%   strch:  Optional Mute strech limit (%):
%
%      ZZ: output data after NMO or un-NMO
%     NMO uses the function nmo0v.
%
%        NOTE:  due to NMO stretch the amplitudes are not consistant from input to output.
%    best use AGC after NMO correction.  See Jon's BEI for details.
%
%

%        Modified by Ran Bachrach, 4-12-2000.

[nt,nx]=size(Tr);
if length(v)==1;V=v+0*[1:nt]';else;V=v;end;
h=waitbar(0,'NMO: Please wait...');
for ix=1:length(offset)
%ix
tr=Tr(:,ix);
ZZ(:,ix)=nmoLv(tr,V,t0,dt,offset(ix),flag,strch);
waitbar(ix/length(offset),h);
end
close(h);



function zz=nmoLv(Tr,V,t0,dt,x,flag,strch,opt);
%%%%%%%%%%%%%%%%%%%%%%%%%%%%%%%%%%%%%%%%%%%%%%
%function zz=nmo0(Tr,V,t0,dt,x,flag,);
%
%This takes an trace and NMO correct it or spary a zero offset trace into an hyperbula
%
% Tr:  Trace at distance x
% t0- two way travel time at x=0 till first live point(use 0 if ther is nodelay)
%  If you don'nt know what to use, use [1:nt]'*dt.
% V- velocity (size(Tr))
% dt- Sampling rate
% zz-  nmo'ed trace
% flag- 0 for nmo correction (make hyperbula flat), 1 for spraying trace
% strch -optional parameter NMO streach (%).  above this streach coef. the data
% is muted.  default is set to no strech mute.
```

```
% opt- large offset correction:
% Note:  Due to NMO streach the amplitude are not consistant from input/output
% Best to use agc after nmo correction.  See Jon's BEI for details
%%%%%%%%%%%%%%%%%%%%%%%%%%%%%%%%%%%%%%%%%
%
if nargin<7;strch=0;end

n=length(Tr);
  zz=Tr*0;
 iz=[1:n]';
  z=t0+dt*(iz-1);
  %size((x./V(iz))),size(z)
  tx=sqrt(z.^2+(x./V(iz)).^2);
  %dT=tx-t0;

  if strch==0
  assrv=tx*0+1;
  else
  assr=tx./(z+dt/1e3);    %alowable sample streatch ratio-for NMO strech limit
  %
  assrv=(assr-1)<=(strch/100);% mute above the strch value
  end

  it1=1+round((tx-t0)/dt);% Round to nearest neighbor
  it= (it1<n).*it1+1;
  %
      if flag==1%undo NMO
       zz(it)=zz(it)+Tr(iz);
      else % Do NMO<=>Hyperbula_flat
     %
         zz(iz)=zz(iz)+Tr(it).*assrv(it);
     end

  return
%%%%%%%%%%%%%%%%%%%%%%%%%%%%%%%%%%%%%%%%%%%%%

spectrum(:,j)=sum(ZZ,2);
end
figure, subplot(1,4,1), imagesc(offset,t1,agx),grid
title('AGC CMP'), xlabel('Offset (m)'), ylabel('Time (sec)')
subplot(1,4,2), imagesc(vel,t1,spectrum),contour(vel,t1,abs(spectrum),15)
colorbar,xlabel('Velocity (m/s)'),grid
set(gca,'ydir','reverse'),title('Velocity Spectrum')
subplot(1,4,3),plot(max(abs(spectrum),[],2),t1,'+-'),grid,set(gca,'ydir','reverse')
axis([min(max(abs(spectrum)))-10 max(max(abs(spectrum)))+10 min(t1) max(t1)])
%axis([min(temp1)-10 max(temp1)+10 min(t1) 1e-7])
title('Max power'),xlabel('Power')
temp2=t1;
for j=1:length(t1);
  for i=1:length(vel);
    if spectrum(j,i)==max(spectrum(j,:)); %if spectrum value=max value of spectrum row
```

```
      temp2(j)=vel(i); %identifies velocity value at max spectrum value along each row
    end
  end
end
subplot(1,4,4),plot(temp2,t1,'+-'),grid,set(gca,'ydir','reverse')
axis([min(vel)-(dv*10) max(vel)+(dv*10) min(t1) max(t1)])
%axis([min(vel)-(dv*10) max(vel)+(dv*10) min(t1) 1e-7])
title('Max velocity'),xlabel('Velocity (m/s)')

inpopt=questdlg('Choose Stacking Velocity?','velocityspectrum','No');
switch inpopt
   case 'Yes'
while temp>1,
defans={'2'}; prompt={'How many velocity values do you need (integer)?'};
dlgtitle='Velocityspectrum';
answer=inputdlg(prompt,dlgtitle,1,defans);
nmv=str2num(answer{1});

hdlg=msgbox('Use Mouse for selecting your specified number of points to create a velocity
function.',...
        'velocityspectrum'); waitfor(hdlg);
figure(2),subplot(1,4,4), [Vstk,tstk]=ginput(nmv);
%%%%%%%%%%%%%%%%%%%%%%%%%%%%%%%%%%%%%%%%%%%%%%%%%%%%%%%%%%%%%%%%%%%%%%%%%%%%%%%%
hold on, plot(Vstk,tstk,'r')
v=1:length(t1); v=v.*0; Vdix=1:nmv; Vdix=Vdix.*0; Vdix(1)=Vstk(1);
for i=2:nmv;
Vdix(i)=sqrt(((Vstk(i)^2*tstk(i))-(Vstk(i-1)^2*tstk(i-1)))/(tstk(i)-tstk(i-1)));
end
for j=1:nmv;
for i=1:round(tstk(j)/dt);
if v(i)==0
v(i)=Vdix(j);
end, end, end
for j=round(tstk(nmv)/dt):length(v);
v(j)=Vdix(nmv);
end
figure(3),hold off, plot(v,t1,'r'), set(gca,'ydir','reverse')
hold on, plot(Vstk,tstk)

inpopt=questdlg('Would you like to make a new velocity spectrum?','velocityspectrum','No');
switch inpopt
   case 'Yes'
temp=2;
   case 'No'
temp=0;
end
end

case 'No'
  Vstk=[];tstk=[];
  return
```

```
end

figure,plot(v,t1,'r'), set(gca,'ydir','reverse')
hold on, plot(Vstk,tstk)

%%%%%%%%%%%%%%%%%%%%%%%%%%%%%%%%%%%%%%%%%%%
% Correct for spherical divergence (v*t)
WSPZfiltx=zeros(size(WSPZfiltx,1),size(WSPZfiltx,2));
for j=1:size(WSPZfiltx,2);
  for k=1:wtable_zero_notopo(j);
    WSPZfiltx(k,j)=WSPZfiltx(k,j)*((WSPZt1(k)/2)*(1.353e8));
  end
  for k=wtable_zero_notopo(j)+1:size(WSPZfiltx,1);
    WSPZfiltx(k,j)=WSPZfiltx(k,j)*(((wtable_zero_notopo_t(j)/2)*(1.353e8))+(((WSPZt1(k)-
wtable_zero_notopo_t(j))/2)*(6.78e7)));
  end
end

%%%%%%%%%%%%%%%%%%%%%%%%%%%%%%%%%%%%%%%%%%%
% Calculate amplitude of reflections from sum of reflection energy
for j=1:401;
  ampwt_sum(j)=sum(abs(WSPZfiltx6_2(wtable_zero_notopo(j)-6:wtable_zero_notopo(j)+7,j)));
  ampcl_sum(j)=sum(abs(WSPZfiltx6_2(clayreflector_zero_notopo(j)-
5:clayreflector_zero_notopo(j)+5,j)));
end
figure
subplot(2,1,1), plot(WSPZx1,ampwt_sum), title('Amplitude of Water Table')
xlabel('Distance (meters)'), ylabel('Summation of Reflection Amplitude')
subplot(2,1,2), plot(WSPZx1,ampcl_sum), title('Amplitude of Clay Layer')
xlabel('Distance (meters)'), ylabel('Summation of Reflection Amplitude')

% Fit polynomials to plots of amplitude values
P=polyfit((1:160),ampwt_sum(1:160),4);
poly_ampwt_west_sum=polyval(P,(1:160));
P=polyfit((245:401),ampwt_sum(245:401),1);
poly_ampwt_east_sum=polyval(P,(245:401));
P=polyfit(1:401,ampcl_sum,4);
poly_ampcl_sum=polyval(P,(1:401));
subplot(2,1,1), hold on, plot(WSPZx1(1:160),poly_ampwt_west_sum,'r')
plot(WSPZx1(245:401),poly_ampwt_east_sum,'r')
subplot(2,1,2), hold on, plot(WSPZx1,poly_ampcl_sum,'r')

% Calculate attenuation using polyfit of Water table to polyfit of clay layer
for j=1:160;
  alpha_west_sum(j)=(log(poly_ampcl_sum(j)/poly_ampwt_west_sum(j)))/...
    (-1*(6.78e7*((clayreflector_zero_notopo_t(j)-wtable_zero_notopo_t(j))/2)));
end
for j=1:157;
  alpha_east_sum(j)=(log(poly_ampcl_sum(j+244)/poly_ampwt_east_sum(j)))/...
    (-1*(6.78e7*((clayreflector_zero_notopo_t(j+244)-wtable_zero_notopo_t(j+244))/2)));
end
```

```
figure
plot(WSPZx1(1:160),alpha_west_sum)
hold on
plot(WSPZx1(245:401),alpha_east_sum), title('Attenuation of EM Wave')
xlabel('Distance (meters)'), ylabel('Attenuation (dB/m)')

% Calculate delta alpha across the transect.  Delta alpha is used later to calculate delta sigma
delta_alpha_west_sum=zeros(1,160);
delta_alpha_west_sum(1)=0;
for j=2:160;
  delta_alpha_west_sum(j)=alpha_west_sum(j)-alpha_west_sum(1);
  end
delta_alpha_east_sum=zeros(1,157);
delta_alpha_east_sum(1)=0;
for j=2:157;
    delta_alpha_east_sum(j)=alpha_east_sum(j)-alpha_east_sum(1);
end

%%%%%%%%%%%%%%%%%%%%%%%%%%%%%%%%%%%%%%%%%%%%%%%%%%%%%%%%%%%%%%%%%%%%%%%%%%%%
% Then run 'sigma_fwd' to calculate delta_sigma and sigma using the calculated delta_alpha
value(s)
%%%%%%%%%%%%%%%%%%%%%%%%%%%%%%%%%%%%%%%%%%%%%%%%%%%%%%%%%%%%%%%%%%%%%%%%%%%%
[sigma_west_sum,delta_sigma_west_sum]=sigma_fwd(50,6.78e7,delta_alpha_west_sum,0.018);
 [sigma_east_sum,delta_sigma_east_sum]=sigma_fwd(50,6.78e7,delta_alpha_east_sum,0.0423);
sigma_west_sum=sigma_west_sum.*((1e6/100)*(0.3^(-2.35)));
sigma_east_sum=sigma_east_sum.*((1e6/100)*(0.3^(-2.35)));
figure, plot(WSPZx1(1:160),sigma_west_sum)
hold on, plot(WSPZx1(245:401),sigma_east_sum)
title('Calculated Specific Conductivity of Groundwater')
xlabel('Distance (meters)'), ylabel('Conductivity (uS/cm)')
axis([0 200 0 700])
figure, plot(WSPZx1(1:160),sigma_west_sum)
hold on, plot(WSPZx1(245:401),sigma_east_sum)
title('Calculated and Measured Specific Conductivity of Groundwater')
xlabel('Distance (meters)'), ylabel('Conductivity (uS/cm)')
axis([0 200 0 705])
hold on

%%%%%%%%%%%%%%%%%%%%%%%%%%%%%%%%%%%%%%%%%%%%%%%%%%%%%%%%%%%%%%%%%%%%%%%%%%%%
function [sigma,delta_sigma]=sigma_fwd(f,v,delta_alpha,ini_cond);
%function [sigma,delta_sigma]=sigma_fwd(f,v,delta_alpha);
% f = frequency (MHz)
% v = velocity (m/s)
% delta_alpha = vector obtained from alpha_eq.m
% sigma = conductivity (S/m)
% delta_sigma = change in conductivity (S/m)
% ini_cond = initial (background) conductivity (S/m)
mu=4e-7*pi;
omega=2*pi*f*1e6;
eps0=1/(((3e8)^2)*mu);
kapa=(3e8/v)^2;
```

```
eps=kapa*eps0;

sigma(1)=ini_cond/(0.3^(-2.35));
for j=1:length(delta_alpha)-1;
  deriv_kim(j)=((sqrt((eps*mu)/2))*sigma(j))/...
    (2*eps^2*omega*(sqrt((sqrt(1+((sigma(j)/(eps*omega))^2)))-1))*...
    (sqrt(1+((sigma(j)/(eps*omega))^2))));
  sigma(j+1)=sigma(1)+(delta_alpha(j+1)/deriv_kim(j));
end

delta_sigma(1)=0;
for j=1:length(sigma)-1;
  delta_sigma(j+1)=sigma(j+1)-sigma(1);
end

%%%%%%%%%%%%%%%%%%%%%%%%%%%%%%%%%%%%%%%%%%%%%%%%%%%%
% June 2000 data
% Weighted avg of sigma measured
plot(WSPZx1(100),190.707,'r*')
plot(WSPZx1(128),298.388,'r*')
plot(WSPZx1(160),530.028,'r*')
plot(WSPZx1(187),400.353,'r*')
plot(WSPZx1(216),453.245,'r*')
plot(WSPZx1(246),388.075,'r*')
plot(WSPZx1(278),427.342,'r*')

% May 1999 Data
% Weighted avg of sigma measured
plot(WSPZx1(160),316.71,'rs')
plot(WSPZx1(187),447.568,'rs')
plot(WSPZx1(216),672.484,'rs')
plot(WSPZx1(246),469.482,'rs')
```

REFERENCES

REFERENCES

Annan, A. P. and Chua, L. T., 1992. Ground Penetrating Radar Performance Predictions. *Ground Penetrating Radar*, edited by Pilon, J. Geologic Survey of Canada, Paper 90-4, pp. 5-13.

Annan, A. P., September 2001. Ground Penetrating Radar Workshop Notes, Sensors & Software Inc.

Atekwana, E. A., Sauck, W. A., and Werkema, D. D., 2000. Investigations of Geoelectrical Signatures at a Hydrocarbon Contaminated Site. *Journal of Applied Geophysics,* Vol. 44, pp. 167-180.

Atekwana, E. A., Sauck, W. A., and Werkema, D. D., 1988. Characterization of a Complex Refinery Groundwater Contamination Plume Using Multiple Geoelectric Methods. *Proceedings of the Symposium on the Application of Geophysics to Engineering and Environmental Problems (SAGEEP 1998),* pp. 675-683.

Bachrach, R. various Matlab® codes. Michigan State University.

Backe, K. R., Lile, O. B., and Lyomov, S. K., 2001. Characterizing Curing Cement Slurries by Electrical Conductivity. *SPE Drilling & Completion*, December, pp. 201-207.

Barber, W. B. and Morey, R., 1994. Radar Detection of Thin Layers of Hydrocarbon Contamination. *Proceedings of the 5th International Conference on Ground Penetrating Radar, Vol. 1, Waterloo Ventre for Groundwater Research,* Waterloo, Ontario, pp. 1215-1228.

Bermejo, J. L., Sauck, W. A., and Atekwana, E. A., 1997. Geophysical Discovery of a New LNAPL Plume at the Former Wurtsmith AFB, Oscoda, Michigan. *Groundwater Monitoring & Remediation.* Vol. 17, pp. 131-137.

Bigalke, J., 2000. A Study Concerning the Conductivity of Porous Rock. *Physics and Chemistry of the Earth*, Vol. 25, No. 2, pp. 189-194.

Boving, T. B. and Grathwohl, P., 2001. Tracer Diffusion Coefficients in Sedimentary Rocks: Correlation to Porosity and Hydraulic Conductivity. *Journal of Contaminant Hydrology*, Vol. 53, pp. 85-100.

Burger, H. R., 1992. Exploration Geophysics of the Shallow Subsurface: New Jersey, Prentice Hall, pp. 144-164.

Chapelle F.H., Haack, S.K., Adriaens, P., Henry, M.A., and Bradley, P.M., 1996. Comparison of Eh and H_2 Measurements for Delineating Redox Processes in a Contaminated Aquifer. *Environmental Science and Technology*, 30: 3565-3569.

Cummings, T. R. and Twenter, F. R., 1986. Assessment of Ground-Water Contamination at Wurtsmith Air Force Base, Michigan, 1982-85. *U.S. Geological Survey, Water Resources Investigation Report 86-4188.*

Fetter, C. W., 1994. Applied Hydrogeology: Prentice Hall, Upper Saddle River, New Jersey.

Fitterman, D. V. and Deszcz-Pan, M., 2001. Saltwater Intrusion in Everglades National Park, Florida Measured by Airborne Electromagnetic Surveys. *First International Conference on Saltwater Intrusion and Coastal Aquifers Monitoring, Modeling, and Management. Essaouira, Morocco, April 23-25.*

Freeze, R. A. and Cherry, J. A., 1979. Groundwater. Prentice Hall, Englewood Cliffs, New Jersey.

Gueguen, Y. and Palciauskus, V., 1994. Introduction to the Physics of Rocks. Princeton University Press, Princeton, New Jersey.

Hwang, S., Shin, J., Park, I., and Lee, S., 2004. Assessment of Seawater Intrusion Using Geophysical Well Logging and Electrical Soundings in a Coastal Aquifer, Youngkwang-gun, Korea. *Exploration Geophysics*, Vol. 35, pp. 99-104.

Kwader, T., 1986. The Use of Geophysical Logs for Determining Formation Water Quality. *Ground Water*, Vol. 24, No. 1, pp. 11-15.

Lendvay, J. M., Sauck, W. A., McCormick, M. L., Barcelona, M. J., Kampbell, D. H., Wilson, J. T., and Adriens, P., 1998. Geophysical Characterization, Redox Zonation, and Contaminant Distribution at a Groundwater/Surface Water Interface. *Water Resources Research*. Vol. 34, No. 12, pp. 3545-3559.

McGuire, J. T., Smith, E. W., Long, D. T., Hyndman, D. W., Haack, S. K., Klug, M. J., and Velbel, M. A., September 2000. Temporal Variation in Parameters Reflecting Terminal-Electron-Accepting Processes in an Aquifer Contaminated With Waste Fuel and Chlorinated Solvents. *Chemical Geology*, Vol. 169, pp. 471-485.

McMahon, P. B. and Chapelle, F. H., 1991. Microbial Production of Organic Acids in Aquitard Sediments and its Role in Aquifer Geochemistry. *Nature*. Vol. 349, pp. 233-235.

Mukerji, T. Various Matlab® codes. Stanford University.

Nash, M. S., Atekwana, E., and Sauck, W. A., 1997. Geophysical Investigation of Anomalous Conductivity at a Hydrocarbon Contaminated Site. *Proceedings of the Symposium on the Application of Geophysical Engineering to Environmental Problems (SAGEEP '97), Environmental and Engineering Geophysical Society*, Englewood, CO, pp. 675-683.

Reynolds, J. M., 1997. An Introduction to Applied and Environmental Geophysics. Chichester, England, John Wiley & Sons Ltd., pp. 355-357.

Sauck, W. A., 2000. A Model For The Resistivity Structure of LNAPL Plumes and Their Environs in Sandy Sediments. *Journal of Applied Geophysics*, Vol. 44, pp. 151-165.

Sauck, W. A., 1998. A Conceptual Model For The Geoelectrical Response Of LNAPL Plumes in Granular Sediments. *Proceedings of the Symposium on the Application of Geophysics to Engineering and Environmental Problems (SAGEEP '98), Chicago, IL*, pp. 805-817.

Sauck, W. A., Atekwana, E. A., and Nash, M. S., 1998. High Conductivities Associated with an LNAPL Plume Imaged by Integrated Geophysical Techniques. *Journal of Environmental and Engineering Geophysics*. Vol. 2, pp. 203-212.

Sensors & Software, 1996. Pulse Ekko User's Guide, Version 1.2.

Sheriff, R. E. and Geldart, L. P., 1995. Exploration Seismology. Cambridge University Press.

Stark, J. R., Cummings, T. R., and Twenter, F. R., 1983. Ground-Water Contamination at Wurtsmith Air Force Base, Michigan. *U.S. Geological Survey, Water Resources Investigation Report 83-4002.*

United States Geological Survey, Water Resources Division, Lansing, Michigan, September 1990. Installation Restoration Program, Phase II – Confirmation / Quantification Stage 2. Final Report for Wurtsmith Air Force Base, Michigan: Hydrogeology Near Wurtsmith Air Force Base, Michigan.

Yilmaz, O., 1987. Seismic Data Processing: Society of Exploration Geophysics, Tulsa, OK.

YSI Incorporated. YSI 6-Series Environmental Monitoring Systems. pp. 171-172.